

# The Adaptive Solution of High-Frequency Helmholtz Equations via Multi-Grade Deep Learning

Peiyao Zhao\*, Rui Wang<sup>†</sup>, Tingting Wu<sup>‡</sup> and Yuesheng Xu<sup>§</sup>

## Abstract

The Helmholtz equation is fundamental to wave modeling in acoustics, electromagnetics, and seismic imaging, yet high-frequency regimes remain challenging due to the “pollution effect”. We propose FD-MGDL, an adaptive framework integrating finite difference schemes with Multi-Grade Deep Learning to efficiently resolve high-frequency solutions. While traditional PINNs struggle with spectral bias and automatic differentiation overhead, FD-MGDL employs a progressive training strategy, incrementally adding hidden layers to refine the solution and maintain stability. Crucially, when using ReLU activation, our algorithm recasts the highly non-convex training problem into a sequence of convex sub-problems. Numerical experiments in 2D and 3D with wavenumbers up to  $\kappa = 200$  show that FD-MGDL significantly outperforms single-grade and conventional neural solvers in accuracy and speed. Applied to an inhomogeneous concave velocity model, the framework accurately resolves wave focusing and caustics, surpassing the 5-point finite difference method in capturing sharp phase transitions and amplitude spikes. These results establish FD-MGDL as a robust, scalable solver for high-frequency wave equations in complex domains.

**Key words:** Deep Neural Networks, Helmholtz Equations, High-Frequency, Adaptive Multi-Grade Deep Learning

## 1 Introduction

Deep learning has rapidly expanded beyond traditional data-driven tasks into AI-driven scientific computing, particularly for solving partial differential equations (PDEs). Representative advances include Physics-Informed Neural Networks (PINNs) [1], which incorporate physical laws into neural network training for forward and inverse problems, and the Fourier Neural Operator (FNO) [2], which learns discretization-invariant mappings between function spaces. Deep learning has also been applied to high-dimensional PDEs through backward stochastic differential equations (BSDEs) [3, 4], mitigating the curse of dimensionality. The Deep Ritz Method [5] and the Deep Galerkin Method (DGM) [6] provide mesh-free neural approaches for variational and high-dimensional problems. More broadly, neural operators [7] generalize neural networks to learn solution operators independent of discretization. Multi-scale architectures such as MscaledDNN [8] incorporate frequency-domain techniques, while the Koopman Neural Operator [9] reformulates PDE dynamics as linear prediction problems to enhance long-term accuracy. Together, these developments demonstrate the transformative potential of deep learning in scientific computing.

Deep neural networks (DNNs) have increasingly been applied to the Helmholtz equation, which arises in wave propagation, acoustics, and electromagnetics. Meshless ray-based DNN methods [10, 11] avoid adaptive meshing and achieve high accuracy in high-frequency regimes. Ray-based learning frameworks [12] extract wave directions from low-frequency solutions to enhance discontinuous Galerkin methods. Hybrid deep learning–multigrid strategies [13] incorporate CNN-based preconditioners for heterogeneous media, and

\*School of Mathematics, Jilin University, Changchun, 130012, P. R. China. E-mail address: zhaopy23@mails.jlu.edu.cn.

<sup>†</sup>School of Mathematics, Jilin University, Changchun 130012, P. R. China. E-mail address: rwang11@jlu.edu.cn. All correspondence should be sent to this author.

<sup>‡</sup>School of Mathematics and Statistics, Shandong Normal University, Jinan 250358, P. R. China. E-mail address: tingtingwu@sdsu.edu.cn.

<sup>§</sup>Department of Mathematics and Statistics, Old Dominion University, Norfolk, VA 23529, United States of America. E-mail address: y1xu@odu.edu. All correspondence should be sent to this author.

deep learning has also been used for inverse design of Helmholtz resonators [14]. PINN-based approaches [15, 16, 17, 18] enable real-time optimization but are typically limited to low-frequency regimes ( $\kappa < 10$ ) due to spectral bias and optimization difficulty. Moreover, many existing neural solvers primarily capture wavenumber-linear oscillations ( $e^{i\kappa x}$ ) rather than more challenging trigonometric variations ( $\sin(\kappa x)$ ), leaving high-frequency, strongly oscillatory regimes insufficiently explored—especially in three dimensions.

Solving Helmholtz equations with large wavenumbers is particularly challenging because the solutions exhibit rapid oscillations. Traditional PINN-based approaches suffer from spectral bias and incur substantial computational cost due to repeated automatic differentiation. Existing DNN-based studies largely focus on two-dimensional problems with relatively small wavenumbers, while three-dimensional Helmholtz equations at large  $\kappa$  remain underexplored.

To address these challenges, we propose a finite difference-based multi-grade deep learning (FD-MGDL) framework. Building on the Multi-Grade Deep Learning (MGDL) methodology [19, 20, 21, 22], which mitigates spectral bias through grade-wise residual learning, we integrate finite difference discretization to replace costly automatic differentiation. The proposed approach targets Helmholtz equations with wavenumbers ranging from 50 to 200. We formulate loss functions for both single-grade deep learning (SGDL) and MGDL, and develop an adaptive strategy that determines the required number of grades based on problem difficulty. The first grade employs a shallow network with two hidden layers, while subsequent grades introduce additional hidden layers to progressively refine the residual. Numerical experiments demonstrate that FD-MGDL consistently outperforms SGDL in accuracy, computational efficiency, and numerical stability across all tested scenarios.

To further evaluate robustness in heterogeneous media, we apply FD-MGDL to a concave velocity model, where the spatially varying velocity creates lensing effects, caustics, and multipathing phenomena. These features generate localized phase transitions and amplitude concentrations that pose significant challenges for numerical solvers. Traditional finite difference and finite element methods often require extremely fine discretization to resolve such effects, leading to high computational cost and potential numerical dispersion. Our 5-point finite difference-based MGDL implementation effectively captures focal regions and sharp oscillations, substantially outperforming the classical 5-point finite difference scheme in both stability and resolution.

The remainder of the paper is organized as follows. Section 2 introduces the FD-MGDL framework. Section 3 presents the adaptive training algorithm and shows that the proposed algorithm enables recasting the highly nonconvex optimization training as a sequence of convex optimizations. Section 4 provides implementation details and a structural ablation study on grade-wise depth allocation. Sections 5 and 6 address two- and three-dimensional problems, respectively. Section 7 compares FD-MGDL with the traditional finite difference method. Section 8 presents experiments on the concave velocity model. Section 9 concludes the paper, and the appendix contains supplementary material.

## 2 FD-MGDL for the Helmholtz equation

In this section, we introduce a finite difference-based MGDL approach for the numerical solution of the Helmholtz equation.

We begin by describing the Helmholtz equation. For each  $d \in \mathbb{N}$ , we define  $\mathbb{N}_d := \{1, 2, \dots, d\}$  and  $\mathbb{Z}_d := \{0, 1, \dots, d - 1\}$ . Let  $\Delta := \sum_{j \in \mathbb{N}_d} \partial^2 / \partial x_j^2$  denote the Laplace operator,  $\kappa$  represent the wavenumber and  $f$  be the source term. The Helmholtz equation, expressed as the elliptic partial differential equation

$$(\Delta + \kappa^2)u = f,$$

represents a time-independent wave equation, where  $u$  is the unknown solution to be learned. We consider the boundary value problem for the Helmholtz equation

$$\begin{cases} (\Delta + \kappa^2(\mathbf{x})) u(\mathbf{x}) = f(\mathbf{x}), & \mathbf{x} \in \Omega, \\ \mathcal{B}(u(\mathbf{x})) = 0, & \mathbf{x} \in \Gamma, \end{cases} \quad (1)$$

where  $\Omega \subset \mathbb{R}^d$  is an open domain with boundary  $\Gamma$ , and  $\mathcal{B}$  is the nonlinear operator representing the boundary conditions.

DNN methods have emerged as a prominent research area for the numerical solution of PDEs. These approaches utilize DNNs as flexible parametric representations of unknown solutions, leveraging their universal approximation properties to handle complex functional forms. A DNN of depth  $D \in \mathbb{N}$  is structured as a sequence of layers: an input layer,  $D - 1$  hidden layers, and a final output layer. Let  $d, s \in \mathbb{N}$  represent the dimensions of the input and output spaces, respectively. For each layer  $j \in \mathbb{Z}_{D+1}$ , we denote the number of neurons by  $d_j$ , with the boundary conditions  $d_0 = d$  and  $d_D = s$ . The network parameters for each layer  $j \in \mathbb{N}_D$  are defined as weight matrix  $\mathbf{W}_j \in \mathbb{R}^{d_j \times d_{j-1}}$  and bias vector  $\mathbf{b}_j \in \mathbb{R}^{d_j}$ . Let  $\sigma : \mathbb{R} \rightarrow \mathbb{R}$  be a fixed activation function, applied componentwise when acting on vectors. For an input vector  $\mathbf{x} = (x_1, \dots, x_d)^\top \in \mathbb{R}^d$ , the transformation performed by the first hidden layer is expressed as

$$\mathcal{H}_1(\{\mathbf{W}_1, \mathbf{b}_1\}; \mathbf{x}) := \sigma(\mathbf{W}_1 \mathbf{x} + \mathbf{b}_1).$$

For a DNN with depth  $D \geq 3$ , the outputs of the subsequent hidden layer are defined recursively for  $j \in \mathbb{N}_{D-2}$  as

$$\mathcal{H}_{j+1}(\{\mathbf{W}_i, \mathbf{b}_i : i \in \mathbb{N}_{j+1}\}; \mathbf{x}) := \sigma(\mathbf{W}_{j+1} \mathcal{H}_j(\{\mathbf{W}_i, \mathbf{b}_i : i \in \mathbb{N}_j\}; \mathbf{x}) + \mathbf{b}_{j+1}).$$

The final output of the DNN is represented by a vector-valued function  $\mathcal{N}_D : \mathbb{R}^d \rightarrow \mathbb{R}^s$ . This map, parameterized by the collection of weights and biases  $\{\mathbf{W}_j, \mathbf{b}_j : j \in \mathbb{N}_D\}$ , is given by:

$$\mathcal{N}_D(\{\mathbf{W}_j, \mathbf{b}_j : j \in \mathbb{N}_D\}; \mathbf{x}) := \mathbf{W}_D \mathcal{H}_{D-1}(\{\mathbf{W}_j, \mathbf{b}_j : j \in \mathbb{N}_{D-1}\}; \mathbf{x}) + \mathbf{b}_D, \quad \mathbf{x} \in \mathbb{R}^d.$$

The PINN framework [1] utilizes a DNN to approximate the solution of a PDE by incorporating the governing equations and boundary conditions directly into the learning process. For the Helmholtz equation (1), the PINN loss function is typically composed of two primary terms: the PDE residual loss and the boundary condition loss. Let  $\Theta := \{\mathbf{W}_j, \mathbf{b}_j : j \in \mathbb{N}_D\}$  denote the network parameters. For interior collocation points  $\{\mathbf{x}_j : j \in \mathbb{N}_{N_{int}}\}$  and boundary points  $\{\tilde{\mathbf{x}}_j : j \in \mathbb{N}_{N_b}\}$ , the components of the loss function are defined as follows:

- **PDE Residual Loss:** Quantifies the degree to which the network output  $\mathcal{N}_D$  satisfies the Helmholtz operator:

$$\mathcal{L}_{PDE}(\Theta) := \frac{1}{N_{int}} \sum_{j \in \mathbb{N}_{N_{int}}} |(\Delta + \kappa^2(\mathbf{x}_j)) \mathcal{N}_D(\Theta; \mathbf{x}_j) - f(\mathbf{x}_j)|^2,$$

- **Boundary Condition Loss:** Enforces the boundary conditions  $\mathcal{B}$  at the specified points:

$$\mathcal{L}_B(\Theta) := \frac{1}{N_b} \sum_{j \in \mathbb{N}_{N_b}} |\mathcal{B}(\mathcal{N}_D(\Theta; \tilde{\mathbf{x}}_j))|^2.$$

The total training objective is generally the weighted sum of these components, minimized through gradient-based optimization.

The selection of training points significantly impacts the convergence and accuracy of the model. Current research highlights two primary strategies:

1. **Random Sampling:** Points are drawn from prescribed probability distributions over the domain [1, 23].
2. **Adaptive Sampling:** Points are iteratively selected in regions where the PDE residual is high to improve the model's local resolution [24, 25].

The training of a PINN is framed as a multi-objective optimization problem. The total loss function is defined as a weighted sum of the PDE residual loss and the boundary condition loss:

$$\mathcal{L}_{PINN}(\Theta) := \lambda_{PDE} \mathcal{L}_{PDE}(\Theta) + \lambda_B \mathcal{L}_B(\Theta). \quad (2)$$

Core components of the model include

- **Weighting Coefficients:** The positive hyperparameters  $\lambda_{PDE}$  and  $\lambda_B$  scale the relative contribution of each loss term.
- **Optimization Dynamics:** Selecting appropriate weights is critical; imbalances between terms can lead to “gradient pathologies”, where a single term dominates the gradient flow and hinders overall convergence.
- **Performance Impact:** Research indicates that the precise tuning of these coefficients dictates the computational efficiency, numerical stability, and convergence accuracy of the model [18, 26, 27].

The objective is to identify the optimal network parameters  $\Theta^*$  by minimizing the total loss over the combined training dataset  $\mathbb{D} := \{\mathbf{x}_j : j \in \mathbb{N}_{N_{int}}\} \cup \{\tilde{\mathbf{x}}_k : k \in \mathbb{N}_{N_b}\}$ :

$$\Theta^* = \arg \min_{\Theta} \mathcal{L}_{PINN}(\Theta).$$

This minimization is typically performed using gradient-based optimization algorithms, such as Adam or L-BFGS, with gradients computed via backpropagation.

Despite its versatility, the standard PINN framework faces two primary challenges:

1. **Weak Enforcement of Constraints:** Because boundary conditions are enforced as soft constraints through the loss function, the resulting solution may exhibit inconsistencies or residuals at the boundaries.
2. **Optimization Stiffness:** The optimization landscape can become excessively “stiff” due to the competing objectives of the PDE and boundary terms. This competition often leads to training instabilities that can impede or entirely prevent convergence [18, 28].

To mitigate these issues, we adopt an approach in which derivative terms, typically computed via Automatic Differentiation (AD), are replaced by Finite Difference (FD) approximations when constructing the PDE loss. This formulation allows the governing equation and boundary conditions to be naturally incorporated into a single discrete system, from which a unified loss function is defined, thereby alleviating issues associated with weak constraint enforcement and optimization stiffness. We emphasize that the MGD framework is flexible and not restricted to this particular setting; depending on the application, it can accommodate both AD- and FD-based formulations [29].

We consider the Helmholtz equation with Dirichlet boundary conditions as a representative example to introduce the proposed method:

$$\begin{cases} (\Delta + \kappa^2(\mathbf{x})) u(\mathbf{x}) = f(\mathbf{x}), & \mathbf{x} \in \Omega, \\ u(\mathbf{x}) = g(\mathbf{x}), & \mathbf{x} \in \Gamma, \end{cases} \quad (3)$$

where  $\Omega := (a, b)^d$ . We approximate the exact solution  $u$  by a DNN  $\mathcal{N}_D(\Theta; \cdot)$  with  $D$  layers, and approximate the Laplace operator  $\Delta$  using a second order central difference scheme. Let  $m \in \mathbb{N}$  and define the set of training points

$$\mathbf{x}_j := (x_{j,i} : i \in \mathbb{N}_d), \text{ where } \mathbf{j} := (j_i : i \in \mathbb{N}_d) \in \mathbb{Z}_{m+2}^d \text{ and } x_{j,i} := a + j_i h \text{ with } h = 1/(m+1).$$

At interior points  $\mathbf{x}_j \in \Omega$ , the solution is approximated by

$$u(\mathbf{x}_j) \approx \mathcal{N}_D(\Theta; \mathbf{x}_j).$$

A key modification is required when the finite difference stencil involves boundary nodes. Instead of evaluating the neural network at boundary points, we directly impose the prescribed boundary data by defining

$$\tilde{\mathcal{N}}_D(\Theta; \mathbf{x}) := \begin{cases} \mathcal{N}_D(\Theta; \mathbf{x}), & \mathbf{x} \in \Omega, \\ g(\mathbf{x}), & \mathbf{x} \in \Gamma. \end{cases}$$

This construction ensures that the boundary conditions are enforced exactly at the discrete level.

Using  $\tilde{\mathcal{N}}_D$ , for the interior points, the second-order central difference approximation of the second derivative at an interior point  $\mathbf{x}_j$  is given by

$$\frac{\partial^2 u}{\partial x_i^2}(\mathbf{x}_j) \approx \frac{\tilde{\mathcal{N}}_D(\Theta; \mathbf{x}_{j+\mathbf{e}_i}) - 2\tilde{\mathcal{N}}_D(\Theta; \mathbf{x}_j) + \tilde{\mathcal{N}}_D(\Theta; \mathbf{x}_{j-\mathbf{e}_i})}{h^2}, \quad i \in \mathbb{N}_d,$$

where  $\mathbf{e}_i$  denotes the  $i$ -th coordinate unit vector in  $\mathbb{R}^d$ .

For each interior training point  $\mathbf{x}_j \in \Omega$ , we define the local residual by

$$\mathcal{E}(\Theta; \mathbf{x}_j) := f(\mathbf{x}_j) - \left[ \sum_{i \in \mathbb{N}_d} \left( \frac{\tilde{\mathcal{N}}_D(\Theta; \mathbf{x}_{j+\mathbf{e}_i}) - 2\tilde{\mathcal{N}}_D(\Theta; \mathbf{x}_j) + \tilde{\mathcal{N}}_D(\Theta; \mathbf{x}_{j-\mathbf{e}_i})}{h^2} \right) + \kappa^2(\mathbf{x}_j)\tilde{\mathcal{N}}_D(\Theta; \mathbf{x}_j) \right].$$

The overall loss function is then defined as

$$\mathcal{L}(\tilde{\mathcal{N}}_D, \Theta) := \frac{1}{m^d} \sum_{\mathbf{j} \in \mathbb{N}_m^d} \mathcal{E}^2(\Theta; \mathbf{x}_j). \quad (4)$$

The finite difference-based SGDL (FD-SGDL) model described above minimizes  $\mathcal{L}(\tilde{\mathcal{N}}_D, \Theta)$  with respect to  $\Theta$ , yielding the optimal parameters  $\Theta^* := \{\mathbf{W}_j^*, \mathbf{b}_j^* : j \in \mathbb{N}_D\}$  and the corresponding DNN approximation  $\mathcal{N}_D(\Theta^*; \cdot)$ . This FD-enhanced construction embeds the boundary conditions into the discrete PDE operator, effectively converting boundary conditions from soft penalty terms into hard constraints. As a result, it eliminates the detrimental competition between  $\mathcal{L}_{PDE}$  and  $\mathcal{L}_B$  in (2), substantially stabilizes the optimization process, and improves solution accuracy in the vicinity of  $\Gamma$ . Moreover, by exploiting information from neighboring grid points, the finite difference formulation has been observed to offer enhanced numerical robustness compared with AD-based residual constructions.

Three remarks regarding the finite difference (FD) component of the FD-MGDL framework are in order:

First, FD-MGDL provides a continuous solution representation, unlike classical FD methods which are restricted to discrete grid points. Although FD schemes approximate derivatives during training, the final neural network is a function defined across the entire domain. This preserves the “mesh-free” advantage, allowing for solution evaluation at any arbitrary coordinate.

Second, the framework generalizes to unstructured domains and scattered point clouds via the Generalized Finite Difference Method (GFDM). By utilizing a local “cloud of points” and Taylor series expansions around each node, the loss function can be constructed without a rigid Cartesian grid. This enables FD-MGDL to resolve complex geometries while maintaining the computational efficiency of FD-based optimization.

Third, while second-order schemes effectively mitigate optimization stiffness and enforce hard constraints, accuracy is inherently limited by truncation error—especially in high-dimensional wave problems. Future research will incorporate higher-order schemes; utilizing larger stencils and refined linear combinations of function values will significantly reduce truncation errors and enhance the precision of the Helmholtz operator approximation.

## Finite Difference-Based Multi-Grade Deep Learning (FD-MGDL)

We introduce the **FD-MGDL framework**, designed to enhance the accuracy and stability of numerical solutions to the Helmholtz equation (3). The core strategy involves decomposing a DNN of total depth  $D$  into  $L$  successive **grades**, where each grade consists of a Shallow Neural Network (SNN). Specifically, the  $l$ -th grade is associated with an SNN  $\mathcal{N}_{D_l}$  of depth  $D_l$ , satisfying  $1 < D_l < D$  and  $\sum_{l \in \mathbb{N}_L} D_l = D + L - 1$ . For each grade  $l$ , we denote by  $\Theta_l := \{\mathbf{W}_{l,j}, \mathbf{b}_{l,j} : j \in \mathbb{N}_{D_l}\}$  the  $l$ -th grade network parameters.

### Grade-1 Initialization:

For the first grade, we employ an SNN  $\mathcal{N}_{D_1}$  with depth  $D_1$ , the initial output  $s_1$  is defined as:

$$s_1(\Theta_1; \mathbf{x}) := \begin{cases} \mathcal{N}_{D_1}(\Theta_1; \mathbf{x}), & \mathbf{x} \in \Omega, \\ g(\mathbf{x}), & \mathbf{x} \in \Gamma. \end{cases}$$

The optimal parameters  $\Theta_1^*$  are determined by minimizing the loss function  $\mathcal{L}(s_1, \Theta_1)$ . To facilitate the hierarchical structure, we decompose this SNN into a **feature map**  $\mathbf{h}_1(\mathbf{x})$  (comprising the first  $D_1 - 1$  layers) and a **linear output layer**:

$$\mathbf{h}_1(\mathbf{x}) := \mathcal{H}_{D_1-1}(\{\mathbf{W}_{1,j}^*, \mathbf{b}_{1,j}^* : j \in \mathbb{N}_{D_1-1}\}; \mathbf{x}), \quad g_1^*(\mathbf{x}) = \mathbf{W}_{1,D_1}^* \mathbf{h}_1(\mathbf{x}) + \mathbf{b}_{1,D_1}^*.$$

## Recursive Multi-Grade Correction:

For subsequent grades  $l \geq 2$ , the framework constructs correction terms recursively. Each grade leverages the feature representations learned in all preceding grades. The  $l$ -th grade output  $g_l$  is defined via the composition of the current SNN with the frozen feature maps of previous grades:

$$g_l(\Theta_l; \mathbf{x}) := \mathcal{N}_{D_l}(\Theta_l; \cdot) \circ \mathbf{h}_{l-1}(\mathbf{x}).$$

The **cumulative approximation** at grade  $l$  is the sum of the current correction and all previous optimal increments:

$$s_l(\Theta_l; \mathbf{x}) := \begin{cases} g_l(\Theta_l; \mathbf{x}) + \sum_{i=1}^{l-1} g_i^*(\mathbf{x}), & \mathbf{x} \in \Omega, \\ g(\mathbf{x}), & \mathbf{x} \in \Gamma. \end{cases} \quad (5)$$

During the optimization of  $\mathcal{L}(s_l, \Theta_l)$ , only the current parameters  $\Theta_l$  are trainable, while all preceding parameters  $\Theta_1^*, \dots, \Theta_{l-1}^*$  remain **fixed**. This prevents optimization pathologies like vanishing gradients by focusing the network's capacity on learning the residual error. After training, the  $l$ -th grade feature representation and solution increment are updated as:

$$\mathbf{h}_l(\mathbf{x}) := \mathcal{H}_{D_l-1}(\{\mathbf{W}_{l,j}^*, \mathbf{b}_{l,j}^* : j \in \mathbb{N}_{D_l-1}\}; \mathbf{h}_{l-1}(\mathbf{x})), \quad g_l^*(\mathbf{x}) = \mathbf{W}_{l,D_l}^* \mathbf{h}_l(\mathbf{x}) + \mathbf{b}_{l,D_l}^*.$$

## Final Approximation:

Upon completing  $L$  grades, the final FD-MGDL numerical approximation is the aggregate of all learned solution increments:

$$s_L^*(\mathbf{x}) = \sum_{i=1}^L g_i^*(\mathbf{x}), \quad \mathbf{x} \in \Omega.$$

A key theoretical property of the proposed FD-MGDL framework is that the optimal loss sequence  $\mathcal{L}(s_l, \Theta_l^*)$ ,  $l \in \mathbb{N}_L$ , is non-increasing. This result extends previous findings in function approximation [19] and integral equation modeling [30] to the domain of differential equations.

For each  $l \in \mathbb{N}_L$  and each  $j \in \mathbb{N}_{D_l}$ , let  $d_{l,j}$  denote the width of the  $j$ -th layer of the neural network at grade  $l$ . To formalize this property, we partition the parameters  $\Theta_l$  of each grade  $l \in \mathbb{N}_L$  into two distinct subspaces:

- Feature Parameters ( $\mathcal{M}_{l,1}$ ): Contains the weights and biases for the first  $D_l - 1$  layers:

$$\mathcal{M}_{l,1} := \left\{ \{\mathbf{W}_{l,j}, \mathbf{b}_{l,j}\}_{j=1}^{D_l-1} : \mathbf{W}_{l,j} \in \mathbb{R}^{d_{l,j} \times d_{l,j-1}}, \mathbf{b}_{l,j} \in \mathbb{R}^{d_{l,j}} \right\}.$$

- Output Parameters ( $\mathcal{M}_{l,2}$ ): Contains the parameters for the final linear layer:

$$\mathcal{M}_{l,2} := \{(\mathbf{W}, \mathbf{b}) : \mathbf{W} \in \mathbb{R}^{d_{l,D_l} \times d_{l,D_l-1}}, \mathbf{b} \in \mathbb{R}^{d_{l,D_l}}\}.$$

Consequently, any  $\Theta_l$  can be uniquely represented as the pair  $(\Theta_{l,1}, \Theta_{l,2})$  with

$$\Theta_{l,1} := \{\mathbf{W}_{l,j}, \mathbf{b}_{l,j} : j \in \mathbb{N}_{D_l-1}\} \in \mathcal{M}_{l,1} \quad \text{and} \quad \Theta_{l,2} := (\mathbf{W}_{l,D_l}, \mathbf{b}_{l,D_l}) \in \mathcal{M}_{l,2}.$$

With the feature function  $\mathbf{h}_l$  fixed from the previous grade, we define the linear operator  $\mathcal{Z}_l : \mathcal{M}_{l,2} \rightarrow C(\Omega)$  as:

$$\mathcal{Z}_l((\mathbf{W}, \mathbf{b})) := \mathcal{A}_h(\mathbf{W}\mathbf{h}_l(\cdot) + \mathbf{b}),$$

where  $\mathcal{A}_h$  is the discrete Helmholtz operator. For any  $v \in C(\Omega)$ ,  $\mathcal{A}_h$  is defined by:

$$(\mathcal{A}_h v)(\mathbf{x}) := \sum_{i=1}^d \frac{v(\mathbf{x} + h\mathbf{e}_i) - 2v(\mathbf{x}) + v(\mathbf{x} - h\mathbf{e}_i)}{h^2} + \kappa^2(\mathbf{x})v(\mathbf{x}). \quad (6)$$

Furthermore, let  $\|\cdot\|_N$  denote the discrete semi-norm computed over the  $m^d$  training points  $\mathbf{x}_j$ :

$$\|v\|_N := \sqrt{\frac{1}{m^d} \sum_{\mathbf{j} \in \mathbb{N}_m^d} |v(\mathbf{x}_j)|^2}, \quad v \in C(\Omega). \quad (7)$$

The following theorem rigorously establishes that the FD-MGDL framework ensures progressive error reduction.

**Theorem 1** (Monotonicity of Loss). *In the FD-MGDL framework, the optimal loss sequence satisfies:*

$$\mathcal{L}(s_{l+1}, \Theta_{l+1}^*) \leq \mathcal{L}(s_l, \Theta_l^*), \quad \text{for all } l \in \mathbb{N}_{L-1}.$$

Moreover, the loss remains strictly decreasing unless the  $(l+1)$ -th grade correction satisfies  $\|\mathcal{A}_h g_{l+1}^*\|_N = 0$ .

See A for the complete proof.

### 3 Adaptive FD-MGDL algorithm

In this section, we propose an adaptive FD-MGDL algorithm for the numerical solution of the Helmholtz equation. This framework incrementally introduces training grades, utilizing an error-driven stopping criterion to automatically determine the optimal network depth. By leveraging the inter-grade error behavior inherent to MGDL, the algorithm adaptively balances approximation accuracy and computational efficiency without requiring the number of grades to be prescribed in advance.

#### (1) Error-Driven Adaptation and Stopping Criterion

As established in Theorem 1, the MGDL framework produces a computable loss sequence that is monotonically non-increasing. This property guarantees that additional grades will not deteriorate the approximation quality, providing a rigorous foundation for adaptive refinement.

In the FD-MGDL setting, the network is trained progressively: each new grade consists of a shallow network composed with the existing, frozen model. Only the parameters of the newly added grade are trained to approximate the current residual. We incorporate an automatic stopping criterion by monitoring the absolute difference between the training losses of two consecutive grades. If the difference falls below a prescribed tolerance  $\epsilon$ , the process terminates; otherwise, a new grade is introduced.

This mechanism offers a distinct advantage over conventional DNN training: instead of redesigning and retraining an entire deep architecture when performance is unsatisfactory, FD-MGDL simply appends a low-complexity correction layer.

#### (2) Hybrid Architectural Design

The architecture of the shallow network at each grade is critical. To avoid the vanishing gradients and optimization pathologies of standard deep networks, we employ a hybrid strategy tailored to the solution’s physics:

##### Grade-1: Capturing Global Oscillations

For the initial grade, we utilize a shallow neural network with two hidden layers and sinusoidal activation functions. This choice is motivated by the success of SIREN [31], which excels at representing the highly oscillatory and periodic solutions characteristic of Helmholtz problems. The sinusoidal prior allows the first grade to capture the dominant wave structure of the solution with high parameter efficiency.

##### Subsequent Grades: Residual Refinement

For all subsequent grades ( $l \geq 2$ ), we switch to shallow networks with a single hidden layer and ReLU activation. This transition is justified by three primary factors:

- **Target Characteristics:** After the first grade, the learning target shifts from the coherent, periodic solution to a residual error. These residuals typically exhibit irregular, non-coherent oscillations and localized fluctuations [21]. The piecewise linear nature of ReLU is better suited for these unstructured patterns.
- **Optimization Stability and Convergence.** On the one hand, optimization algorithms for two-layer networks have been shown to guarantee convergence under appropriate conditions [32]. On the other hand, two-layer ReLU networks admit exact convex reformulations [33, 34, 35]. Together, these results ensure that each refinement step corresponds to a stable and reliable optimization problem, while maintaining sufficient expressive power and avoiding the instabilities associated with deep nonlinear architectures.
- **Vanishing Approximation Error:** Within the MGDL framework, the use of a single-hidden-layer ReLU networks at each grade has been shown to yield vanishing approximation error in the limit [36]. This theoretical guarantee establishes the asymptotic consistency of the multi-grade approach, ensuring that the cumulative model can approximate the exact solution arbitrarily well as the number of grades increases.

In light of the preceding discussion, we propose an adaptive MGDL algorithm for the numerical solution of the Helmholtz Equation.

---

**Algorithm 1** Adaptive FD-MGDL for the Helmholtz Equation

---

**Require:** Helmholtz equation (3), training points  $\{\mathbf{x}_j\}$ , and error tolerance  $\epsilon > 0$ .

**Phase I: Grade-1 Initialization**

- 1: Initialize SNN  $s_1(\Theta_1; \mathbf{x})$  with parameters  $\Theta_1$ .
- 2: Solve  $\Theta_1^* = \arg \min_{\Theta_1} \mathcal{L}(s_1, \Theta_1)$  and set  $\mathcal{L}_1^* = \mathcal{L}(s_1, \Theta_1^*)$ .
- 3: Set  $l = 1$  and  $\mathcal{L}_0^* = \infty$  (or a sufficiently large value).

**Phase II: Adaptive Residual Refinement**

- 4: **while**  $|\mathcal{L}_l^* - \mathcal{L}_{l-1}^*| > \epsilon$  **do**
  - 5:      $l \leftarrow l + 1$ .
  - 6:     **Freeze** optimal parameters  $\{\Theta_1^*, \dots, \Theta_{l-1}^*\}$ .
  - 7:     Initialize  $l$ -th grade SNN  $s_l(\Theta_l; \mathbf{x})$  with parameters  $\Theta_l$ .
  - 8:     Construct cumulative model  $s_l(\Theta_l; \mathbf{x})$  per (5).
  - 9:     Solve  $\Theta_l^* = \arg \min_{\Theta_l} \mathcal{L}(s_l, \Theta_l)$  and set  $\mathcal{L}_l^* = \mathcal{L}(s_l, \Theta_l^*)$ .
  - 10: **end while**
  - 11: **Return** final numerical solution  $s_L^*(\mathbf{x}) = \sum_{i=1}^L g_i^*(\mathbf{x})$ .
- 

Below we reformulate the nonconvex optimization problem arising in the FD-MGDL framework with two-layer ReLU networks at each grade as a sequence of convex optimization subproblems, following the approach of [33].

For a grade  $l \geq 2$ , we model the correction term using a two-layer ReLU network  $\mathcal{N}_{2_l} : \mathbb{R}^{d_{l-1}, D_{l-1}-1} \rightarrow \mathbb{R}$  with  $m_l$  hidden neurons, defined as:

$$\mathcal{N}_{2_l}(\mathbf{t}_l) = \sum_{j=1}^{m_l} \alpha_{lj} (\mathbf{t}_l^\top \mathbf{w}_{lj})_+,$$

where  $\mathbf{t}_l \in \mathbb{R}^{d_{l-1}, D_{l-1}-1}$  represents the input feature vector for grade  $l$ , while  $\mathbf{w}_{lj} \in \mathbb{R}^{d_{l-1}, D_{l-1}-1}$  and  $\alpha_{lj} \in \mathbb{R}$  denote the hidden-layer weights and output layer coefficients, respectively.

**Data and Target Formulation:** To organize the training points  $\mathbf{x}_j$  ( $\mathbf{j} \in \mathbb{N}_m^d$ ), we fix an ordering via a bijection  $\phi : \mathbb{N}_{m^d} \rightarrow \mathbb{N}_m^d$ . We define the feature data matrix  $\mathbf{X}_l \in \mathbb{R}^{m^d \times d_{l-1}, D_{l-1}-1}$  by collecting the feature representations from the preceding grade:

$$\mathbf{X}_l := [\mathbf{h}_{l-1}(\mathbf{x}_{\phi(1)}), \mathbf{h}_{l-1}(\mathbf{x}_{\phi(2)}), \dots, \mathbf{h}_{l-1}(\mathbf{x}_{\phi(m^d)})]^\top.$$

The training target for grade  $l$  is the optimal residual vector  $\mathbf{e}_{l-1}^*$  inherited from grade  $l-1$ :

$$\mathbf{e}_{l-1}^* := [e_{l-1}^*(\mathbf{x}_{\phi(1)}), e_{l-1}^*(\mathbf{x}_{\phi(2)}), \dots, e_{l-1}^*(\mathbf{x}_{\phi(m^d)})]^\top \in \mathbb{R}^{m^d}.$$

**The Optimization Problem:** Training the network at grade  $l$  thus involves solving the following non-convex optimization problem:

$$\min_{\{\mathbf{w}_{lj}, \alpha_{lj}\}_{j=1}^{m_l}} \left\| \mathbf{e}_{l-1}^* - \mathcal{A}_h \sum_{j=1}^{m_l} (\mathbf{X}_l \mathbf{w}_{lj})_+ \alpha_{lj} \right\|_2^2, \quad (8)$$

where the discrete Helmholtz operator  $\mathcal{A}_h$  is applied component-wise to the resulting vector. This structure reveals that while the objective is non-convex in the weights  $\mathbf{w}_{lj}$ , it maintains a specific multilinear form that facilitates the convex reformulation discussed in the subsequence.

We now define the equivalent convex optimization problem. For any weight vector  $\mathbf{w} \in \mathbb{R}^{d_{l-1}, D_{l-1}-1}$ , let  $\text{Diag}(1[\mathbf{X}_l \mathbf{w} \geq 0])$  be a diagonal matrix, where  $1[\cdot]$  is the element-wise indicator function:

$$1[\mathbf{X}_l \mathbf{w} \geq 0] = \left( 1[\mathbf{h}_{l-1}(\mathbf{x}_{\phi(1)})^\top \mathbf{w} \geq 0], \dots, 1[\mathbf{h}_{l-1}(\mathbf{x}_{\phi(m^d)})^\top \mathbf{w} \geq 0] \right)^\top \in \{0, 1\}^{m^d}.$$

Let  $\mathbf{D}_{l1}, \dots, \mathbf{D}_{lP_l}$  be the set of all  $P_l$  distinct diagonal matrices generated as  $\mathbf{w}$  varies over  $\mathbb{R}^{d_{l-1}, D_{l-1}-1}$ . Each matrix  $\mathbf{D}_{li}$  corresponds to a unique *convex polyhedral cone*  $K_{li}$ , defined as:

$$K_{li} := \left\{ \mathbf{w} \in \mathbb{R}^{d_{l-1}, D_{l-1}-1} : (\mathbf{X}_l \mathbf{w})_k \geq 0, \text{ if } (\mathbf{D}_{li})_{kk} = 1; (\mathbf{X}_l \mathbf{w})_k < 0, \text{ if } (\mathbf{D}_{li})_{kk} = 0, k \in \mathbb{N}_{m^d} \right\}. \quad (9)$$

Geometrically, the collection of hyperplanes  $\mathbf{h}_{l-1}(\mathbf{x}_{\phi(k)})^\top \mathbf{w} = 0$  partition the weight space  $\mathbb{R}^{d_{l-1}, D_{l-1}-1}$  into these  $P_l$  cones. For a given feasible solution  $\{\mathbf{w}_{lj}, \alpha_{lj}\}_{j=1}^{m_l}$  of problem (8), we can group the neurons according to which cone their weight vector lies in. For each  $i \in \mathbb{N}_{P_l}$ , we set

$$S_{li} := \{j \in \mathbb{N}_{m_l} : \mathbf{w}_{lj} \in K_{li}\}.$$

The sets  $S_{li}$ ,  $i \in \mathbb{N}_{P_l}$  form a partition of the index set  $\mathbb{N}_{m_l}$ , that is,

$$\bigcup_{i=1}^{P_l} S_{li} = \mathbb{N}_{m_l} \quad \text{and} \quad S_{li} \cap S_{li'} = \emptyset \quad \text{for } i \neq i'.$$

Therefore, the network output can be rewritten as

$$\mathcal{A}_h \sum_{j=1}^{m_l} (\mathbf{X}_l \mathbf{w}_{lj})_+ \alpha_{lj} = \mathcal{A}_h \sum_{i=1}^{P_l} \sum_{j \in S_{li}} (\mathbf{X}_l \mathbf{w}_{lj})_+ \alpha_{lj}. \quad (10)$$

By definition (9) of  $K_{li}$ , we have for each  $j \in S_{li}$  and each  $k \in \mathbb{N}_{m^d}$  that if  $(\mathbf{D}_{li})_{kk} = 1$ , then  $(\mathbf{X}_l \mathbf{w}_{lj})_k \geq 0$ , and if  $(\mathbf{D}_{li})_{kk} = 0$ , then  $(\mathbf{X}_l \mathbf{w}_{lj})_k < 0$ . These inequalities immediately yield that

$$(\mathbf{X}_l \mathbf{w}_{lj})_+ = \mathbf{D}_{li} \mathbf{X}_l \mathbf{w}_{lj}, \quad j \in S_{li}. \quad (11)$$

Substituting equation (11) into the right hand side of equation (10) leads to

$$\mathcal{A}_h \sum_{j=1}^{m_l} (\mathbf{X}_l \mathbf{w}_{lj})_+ \alpha_{lj} = \mathcal{A}_h \sum_{i=1}^{P_l} \mathbf{D}_{li} \mathbf{X}_l \left( \sum_{j \in S_{li}} \alpha_{lj} \mathbf{w}_{lj} \right). \quad (12)$$

For each  $i \in \mathbb{N}_{P_l}$ , we introduce auxiliary vectors that aggregate the positive and negative contributions within each cone:

$$\mathbf{v}_{li} := \sum_{j \in S_{li}, \alpha_{lj} \geq 0} \alpha_{lj} \mathbf{w}_{lj}, \quad \mathbf{u}_{li} := - \sum_{j \in S_{li}, \alpha_{lj} < 0} \alpha_{lj} \mathbf{w}_{lj}.$$

Substituting

$$\sum_{j \in S_{li}} \alpha_{lj} \mathbf{w}_{lj} = \mathbf{v}_{li} - \mathbf{u}_{li}$$

into equation (12) yields that

$$\mathcal{A}_h \sum_{j=1}^{m_l} (\mathbf{X}_l \mathbf{w}_{lj})_+ \alpha_{lj} = \mathcal{A}_h \sum_{i=1}^{P_l} \mathbf{D}_{li} \mathbf{X}_l (\mathbf{v}_{li} - \mathbf{u}_{li}).$$

Since  $\mathbf{v}_{li}$ ,  $\mathbf{u}_{li}$  are non-negative linear combinations of weight vectors within  $K_{li}$ , they inherit the cone membership property. Specifically, they satisfy the linear constraints

$$(2\mathbf{D}_{li} - \mathbf{I}) \mathbf{X}_l \mathbf{v}_{li} \geq 0, \quad (2\mathbf{D}_{li} - \mathbf{I}) \mathbf{X}_l \mathbf{u}_{li} \geq 0.$$

This transformation shows that every feasible solution of the non-convex problem (8) can be mapped to a feasible solution of a convex optimization problem with exactly the same objective value. This motivates the definition of the equivalent convex optimization problem:

$$\begin{aligned} \min_{\{\mathbf{v}_{li}, \mathbf{u}_{li}\}_{i=1}^{P_l}} & \left\| \mathbf{e}_{l-1}^* - \mathcal{A}_h \sum_{i=1}^{P_l} \mathbf{D}_{li} \mathbf{X}_l (\mathbf{v}_{li} - \mathbf{u}_{li}) \right\|_2^2 \\ \text{subject to} & (2\mathbf{D}_{li} - \mathbf{I}) \mathbf{X}_l \mathbf{v}_{li} \geq 0, \quad (2\mathbf{D}_{li} - \mathbf{I}) \mathbf{X}_l \mathbf{u}_{li} \geq 0, \quad i \in \mathbb{N}_{P_l}. \end{aligned} \quad (13)$$

The linear constraints in (13) ensure that the vectors  $\mathbf{v}_{li}$  and  $\mathbf{u}_{li}$  remain within their respective cones  $K_{li}$ , effectively transforming the original non-convex search for weights into a structured search across a fixed arrangement of linear regions. Since every non-convex solution has a corresponding convex counterpart with the same objective, taking the minimum over the convex set provides a global lower bound.

The following theorem characterizes the equivalence between the non-convex optimization problem (8) and the convex reformulation (13). Specifically, it establishes that the convex problem serves as a global lower bound for the non-convex objective. Furthermore, when the hidden layer width  $m_l$  is sufficiently large, the duality gap vanishes—the optimal values of both problems coincide, and the global minimizers of the neural network can be recovered explicitly from the solution of the convex program.

**Theorem 2** (Convex–Nonconvex Equivalence). *Let  $P_{\text{nc}}^*$  and  $P_c^*$  denote the optimal values of the non-convex training problem (8) and the convex reformulation (13), respectively. The following properties hold:*

1. **Lower Bound:** *For any network width  $m_l \geq 1$ , the convex problem provides a global lower bound such that  $P_{\text{nc}}^* \geq P_c^*$ .*
2. **Global Optimality and Construction:** *Let  $\{(\mathbf{v}_{li}^*, \mathbf{u}_{li}^*)\}_{i=1}^{P_l}$  be an optimal solution to the convex program (13). If the network width satisfies*

$$m_l \geq m_l^* := \sum_{i=1}^{P_l} (1[\mathbf{v}_{li}^* \neq \mathbf{0}] + 1[\mathbf{u}_{li}^* \neq \mathbf{0}]),$$

*then the duality gap vanishes ( $P_{\text{nc}}^* = P_c^*$ ).*

*Furthermore, a globally optimal solution  $\{\mathbf{w}_{lj}^*, \alpha_{lj}^*\}_{j=1}^{m_l}$  for the non-convex problem (8) is explicitly constructed as follows:*

- *For each  $i \in \{1, \dots, P_l\}$  where  $\mathbf{v}_{li}^* \neq \mathbf{0}$ :*

$$\left( \mathbf{w}_{lj_{1,i}}^*, \alpha_{lj_{1,i}}^* \right) = \left( \frac{\mathbf{v}_{li}^*}{\|\mathbf{v}_{li}^*\|}, \|\mathbf{v}_{li}^*\| \right)$$

- *For each  $i \in \{1, \dots, P_l\}$  where  $\mathbf{u}_{li}^* \neq \mathbf{0}$ :*

$$\left( \mathbf{w}_{lj_{2,i}}^*, \alpha_{lj_{2,i}}^* \right) = \left( \frac{\mathbf{u}_{li}^*}{\|\mathbf{u}_{li}^*\|}, -\|\mathbf{u}_{li}^*\| \right).$$

Here,  $\{j_{1,i}\}$  and  $\{j_{2,i}\}$  are distinct neuron indices. The remaining  $m_l - m_l^*$  neurons are set to  $(\mathbf{0}, 0)$ .

The complete proof is provided in B.

The established convex–nonconvex equivalence ensures that, with sufficient network width, the non-convex training of a two-layer ReLU network shares the same optimal value as a structured convex program. Within the FD-MGDL framework, this insight serves two primary roles:

- **Algorithmic Flexibility:** It provides an alternative path to global optimality via convex solvers, bypassing the initialization sensitivity of non-convex optimization.
- **Structural Certification:** More importantly, it certifies the **structural benignity** of the non-convex landscape. As established in [34], the global optima of the convex program correspond to the stationary points of the non-convex objective. This suggests that backpropagation acts as an effective heuristic for the underlying convex structure, with Stochastic Gradient Descent (SGD) consistently converging to the convex optimum regardless of initialization.

Consequently, this equivalence justifies using standard non-convex training at each grade, ensuring that the refinement of the Helmholtz solution remains a principled and stable task.

## 4 Implementation Details and Structural Ablation Study

This section details the implementation of Algorithm 1, provides its justification, and presents a structural ablation study investigating the influence of network depth on the multi-grade learning process.

### 4.1 Implementation Details

**Optimization and Initialization.** For each grade  $l$ , the optimization problem is solved using the Adam optimizer with Xavier initialization. We apply an exponential learning rate decay schedule where the learning rate at epoch  $k$  is:

$$t_k := t_{\max} \exp(-\gamma k), \quad \gamma := \frac{\ln(t_{\max}/t_{\min})}{K},$$

where  $K$  is the total number of epochs, and  $t_{\max}$  and  $t_{\min}$  are the prescribed maximum and minimum learning rates. Training terminates if  $K$  is reached or if the change in training loss between iterations falls below a tolerance  $\epsilon$ .

**Evaluation Metrics.** To assess accuracy, we use the Relative Squared Error (RSE). For a network  $\mathcal{N}$  predicting  $\hat{\mathbf{y}}_\ell := \mathcal{N}(\mathbf{x}_\ell)$  given inputs  $\mathbf{x}_\ell$  ( $\ell \in \mathbb{N}_N$ ), the RSE is:

$$\text{RSE} := \frac{\sum_{\ell \in \mathbb{N}_N} \|\hat{\mathbf{y}}_\ell - \mathbf{y}_\ell\|_2^2}{\sum_{\ell \in \mathbb{N}_N} \|\mathbf{y}_\ell\|_2^2}.$$

We denote errors on training and testing sets as TrRSE and TeRSE, respectively. Computational efficiency is measured via Accumulated Computational Time (AC Time):

$$\text{AC time} := \begin{cases} \sum_{j=1}^i t_j, & \text{for MGDL (up to grade } i), \\ t_{\text{full}}, & \text{for other methods,} \end{cases}$$

where  $t_j$  denotes the training time for the  $j$ -th grade in MGDL, and  $t_{\text{full}}$  is the total training time for the competing methods.

### 4.2 Theoretical Motivation: Convexity and Stability

While the FD-MGDL framework utilizes the Adam optimizer to solve non-convex loss functions for efficiency, its performance is theoretically grounded in the convex subproblem formulation described in (13). This bridge between non-convex optimization and convex theory is critical for two primary reasons:

- **Computational Scalability:** Directly solving the convex subproblems via Quadratic Programming (QP) or specialized convex solvers is computationally prohibitive for large-scale 2D and 3D Helmholtz problems. This is primarily due to the extreme memory overhead and high dimensionality inherent in the activation patterns of large-scale systems. While the direct translation of Theorem 2 into specialized solvers remains a subject for further investigation, the theorem currently serves to justify why gradient-based methods can effectively navigate the search space without the need for prohibitive convex solvers.
- **Theoretical Guarantee:** Theorem 2 establishes that with sufficient network width, the non-convex optimization landscape possesses a benign structure—it contains no “bad” local minima.

Consequently, gradient-based methods like Adam act as implicit solvers for the underlying convex program. This theoretical consistency ensures stable convergence even at high wavenumbers—conditions under which traditional single-grade methods (such as FD-SGDL) typically stagnate due to optimization stiffness. By decomposing the problem into multiple shallow grades, FD-MGDL leverages this benign landscape to refine the solution progressively and reliably.

### 4.3 Adaptive Nature of the FD-MGDL Framework

The adaptive nature of FD-MGDL is governed by the tolerance threshold  $\epsilon$ , which triggers the transition between successive grades. The robustness of this mechanism is supported by the monotonicity of the loss function (Theorem 2.1).

**Theoretical Robustness:** Theorem 2.1 guarantees that the training loss  $\mathcal{L}$  is non-increasing as the grade level  $l$  increases. This ensures that adding a new grade serves as a refinement step that either reduces the residual or maintains the current error level. Thus, the threshold  $\epsilon$  acts as a criterion for identifying diminishing returns rather than a volatile hyperparameter that might risk instability.

In practice, the optimal  $\epsilon$  is coupled with the wavenumber  $\kappa$  and domain complexity. We adopt a monitoring strategy based on the TrRSE: if the error plateaus,  $\epsilon$  is increased to terminate the grade-switching early and save computation; if a downward trend persists,  $\epsilon$  is decreased to introduce new grades and capture high-frequency features more accurately.

**Learning Rate Selection and Stability:** Because parameters from previous grades are frozen, each grade constitutes an independent optimization problem. We perform a grid search over learning rates  $\{10^{-1}, \dots, 10^{-4}\}$  to identify optimal  $t_{\max}$  and  $t_{\min}$ .

Interestingly, as the grade index  $l$  increases, the magnitude of the residual  $\|e_{l-1}^*\|_N$  typically decreases. This indicates that subsequent grades are fine-tuning the solution on a progressively “smaller signal,” which provides a protective, stabilizing effect. This built-in stability ensures the final solution remains robust even with minor variations in the learning rate.

### 4.4 Structural Ablation Study

To assess the effectiveness of the proposed adaptive algorithm, we conduct ablation studies focusing on the depth of the shallow networks used in the multi-grade learning process. Specifically, we consider the following two-dimensional Helmholtz problem:

$$\begin{cases} \frac{\partial^2 u}{\partial x_1^2} + \frac{\partial^2 u}{\partial x_2^2} + \kappa^2 u(x_1, x_2) = 0, & (x_1, x_2) \in \Omega, \\ u(x_1, x_2) = 0, & (x_1, x_2) \in \Gamma_1 := \{0\} \times (0, 1), \\ u(x_1, x_2) = 0, & (x_1, x_2) \in \Gamma_2 := (0, 1) \times \{0\}, \\ u(x_1, x_2) = \sin\left(\frac{\sqrt{2}}{2}\kappa\right) \sin\left(\frac{\sqrt{2}}{2}\kappa x_2\right), & (x_1, x_2) \in \Gamma_3 := \{1\} \times (0, 1), \\ u(x_1, x_2) = \sin\left(\frac{\sqrt{2}}{2}\kappa x_1\right) \sin\left(\frac{\sqrt{2}}{2}\kappa\right), & (x_1, x_2) \in \Gamma_4 := (0, 1) \times \{1\}, \end{cases} \quad (14)$$

where  $\kappa = 50$ .

To isolate the effect of network depth allocation, we systematically vary the number of hidden layers within each grade while keeping all other hyperparameters and training settings fixed. This study is designed to investigate how network depth influences the accuracy, convergence behavior, and computational efficiency of the MGDL framework. We evaluate the effectiveness of the following structures:

1. MGDL-1 (Adaptive FD-MGDL):

$$\text{Grade 1 : } [2] \rightarrow [256] \times 2 \rightarrow [1]$$

$$\text{Grade } j : [2] \rightarrow [256]_F \times j \rightarrow [256] \rightarrow [1], \quad j = 2, 3, \dots, L.$$

MGDL-1 follows the Adaptive FD-MGDL algorithm described in Algorithm 1, where the total number of grades  $L$  are determined automatically during training according to a loss-based convergence criterion. For the Helmholtz problem (14), the adaptive procedure terminates at  $L = 6$ , when the loss reduction between successive grades falls below the prescribed tolerance.

2. MGDL-2:

$$\text{Grade 1 : } [2] \rightarrow [256] \times 2 \rightarrow [1]$$

$$\text{Grade 2 : } [2] \rightarrow [256]_F \times 2 \rightarrow [256] \times 2 \rightarrow [1]$$

$$\text{Grade 3 : } [2] \rightarrow [256]_F \times 4 \rightarrow [256] \times 3 \rightarrow [1].$$

3. MGDL-3:

$$\text{Grade 1 : } [2] \rightarrow [256] \times 3 \rightarrow [1]$$

$$\text{Grade 2 : } [2] \rightarrow [256]_F \times 3 \rightarrow [256] \times 2 \rightarrow [1]$$

$$\text{Grade 3 : } [2] \rightarrow [256]_F \times 5 \rightarrow [256] \times 2 \rightarrow [1].$$

MGDL-2 and MGDL-3 are constructed as controlled variants of MGDL-1 by redistributing a comparable total number of hidden layers into fewer grades with deeper per-grade architectures.

Table 1: Performance comparison of MGDL-1, MGDL-2 and MGDL-3 for solving 2D Helmholtz equation (14).

Structure	Grade	Epochs	$t_{\max}$	$t_{\min}$	AC time (s)	TrRSE	TeRSE
MGDL-1	Grade 1	400	$10^{-1}$	$10^{-2}$	489	$5.62 \times 10^{-1}$	$5.64 \times 10^{-1}$
	Grade 2	3,000	$10^{-2}$	$10^{-3}$	2,443	$6.98 \times 10^{-4}$	$7.07 \times 10^{-4}$
	Grade 3	3,000	$10^{-3}$	$10^{-4}$	3,736	$5.49 \times 10^{-4}$	$5.50 \times 10^{-4}$
	Grade 4	2,500	$10^{-3}$	$10^{-3}$	4,798	$5.41 \times 10^{-4}$	$5.43 \times 10^{-4}$
	Grade 5	2,500	$10^{-3}$	$10^{-3}$	5,852	$5.37 \times 10^{-4}$	$5.38 \times 10^{-4}$
	Grade 6	1,000	$10^{-3}$	$10^{-3}$	6,272	$5.37 \times 10^{-4}$	$5.37 \times 10^{-4}$
MGDL-2	Grade 1	2,000	$10^{-1}$	$10^{-2}$	2,456	$3.99 \times 10^{-1}$	$4.01 \times 10^{-1}$
	Grade 2	2,000	$10^{-2}$	$10^{-2}$	3,953	$6.85 \times 10^{-3}$	$5.86 \times 10^{-3}$
	Grade 3	2,000	$10^{-3}$	$10^{-3}$	6,083	$4.61 \times 10^{-3}$	$4.77 \times 10^{-3}$
MGDL-3	Grade 1	2,000	$10^{-1}$	$10^{-4}$	3,890	$2.03 \times 10^{-2}$	$2.07 \times 10^{-2}$
	Grade 2	2,000	$10^{-3}$	$10^{-3}$	5,755	$5.56 \times 10^{-4}$	$5.64 \times 10^{-4}$
	Grade 3	2,000	$10^{-3}$	$10^{-3}$	7,526	$5.43 \times 10^{-4}$	$5.43 \times 10^{-4}$

The results in Table 1 and Figure 1 illustrate how different depth allocation strategies affect the performance of the MGDL framework across successive grades. Among the three configurations, MGDL-1—based on the adaptive, grade-wise architecture design—achieves the lowest training and testing errors, reaching final TrRSE and TeRSE values of  $5.37 \times 10^{-4}$  over six grades. Notably, the error reduction in MGDL-1 is progressive and stable across grades, indicating that the adaptive introduction of shallow networks effectively captures the residual error at each grade without inducing instability in the optimization process.

This conclusion is further supported by the evolution of the training loss curves. In particular, MGDL-1 exhibits a smooth and nearly monotonic decay of the training loss as the grade index increases, reflecting a stable and well-conditioned optimization trajectory. In contrast, MGDL-2 and MGDL-3, which redistribute a comparable total network depth into fewer grades with deeper per-grade architectures, display inferior

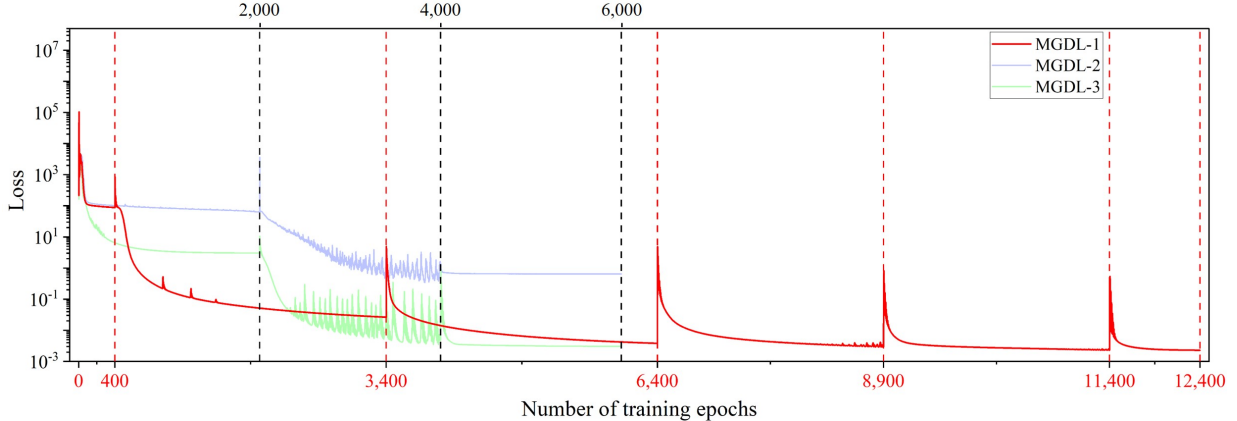


Figure 1: Performance comparison of training loss curves of FD-MGDL with different structures for solving 2D Helmholtz equation (14).

training behavior. Although MGDL-2 achieves a moderate error reduction in the initial grades, its final accuracy remains nearly an order of magnitude worse than that of MGDL-1. Moreover, its training loss curve exhibits noticeable oscillations, indicating unstable optimization dynamics. This instability can be attributed to the increased network depth within each grade, which exacerbates the nonconvexity of the loss landscape and hinders effective residual fitting. MGDL-3 attains a final accuracy comparable to that of MGDL-1; however, this improvement comes at the expense of substantially higher computational cost, as reflected by the longest accumulated training time among the three configurations. In addition, its training loss curve also displays oscillatory behavior, suggesting that deeper per-grade networks do not provide a clear advantage in optimization stability and may instead reduce training efficiency.

Overall, these results demonstrate that the proposed adaptive, grade-wise shallow network design achieves a favorable balance among accuracy, optimization stability, and computational efficiency. The comparison confirms that distributing model capacity across multiple shallow grades—rather than concentrating depth within individual grades—is more effective for solving high-frequency Helmholtz problems within the MGDL framework, thereby justifying the architectural choices adopted in this work.

## 5 Two-dimensional Helmholtz Equations

In this section, we consider the numerical solution of two-dimensional Helmholtz equations with Dirichlet boundary conditions at large wavenumbers:

$$\begin{cases} \frac{\partial^2 u}{\partial x_1^2} + \frac{\partial^2 u}{\partial x_2^2} + \kappa^2 u(x_1, x_2) = f(x_1, x_2), & (x_1, x_2) \in \Omega, \\ u(x_1, x_2) = g(x_1, x_2), & (x_1, x_2) \in \Gamma. \end{cases} \quad (15)$$

We compare the performance of the proposed FD-MGDL method with several representative approaches, including FD-SGDL, Mscale [8], FBPINN [37], SIREN [31], PINN [1], and Pre-PINN [38].

Specifically, **Mscale** employs a multi-scale neural network architecture based on frequency scaling to enhance the approximation of high-frequency components; **FBPINN** adopts a domain decomposition framework in which the solution is represented as a sum of neural-network-based basis functions with compact support over overlapping subdomains; **SIREN** utilizes sinusoidal activation functions to construct implicit neural representations capable of accurately capturing oscillatory solutions and their derivatives; and **Pre-PINN** reformulates PINN training from an operator preconditioning perspective to improve convergence behavior under ill-conditioned settings.

## 5.1 Highly Oscillatory Sine Solution

We first consider the same two-dimensional Helmholtz problem with a highly oscillatory sine solution as in the previous section, now employed as a benchmark to evaluate and compare different numerical methods in the high-wavenumber regime. The source term is set to zero,

$$f(x_1, x_2) = 0, \quad (x_1, x_2) \in \Omega = (0, 1)^2.$$

Dirichlet boundary conditions are imposed on the boundary components  $\Gamma = \{\Gamma_1, \Gamma_2, \Gamma_3, \Gamma_4\}$  as

$$g(x_1, x_2) = \begin{cases} 0, & \text{if } (x_1, x_2) \in \Gamma_1 := \{0\} \times (0, 1); \\ 0, & \text{if } (x_1, x_2) \in \Gamma_2 := (0, 1) \times \{0\}; \\ \sin\left(\frac{\sqrt{2}}{2}\kappa\right) \sin\left(\frac{\sqrt{2}}{2}\kappa x_2\right), & \text{if } (x_1, x_2) \in \Gamma_3 := \{1\} \times (0, 1); \\ \sin\left(\frac{\sqrt{2}}{2}\kappa x_1\right) \sin\left(\frac{\sqrt{2}}{2}\kappa\right), & \text{if } (x_1, x_2) \in \Gamma_4 := (0, 1) \times \{1\}, \end{cases}$$

where  $\kappa$  is a constant wavenumber. The unique exact solution of problem (15) is

$$u(x_1, x_2) = \sin\left(\frac{\sqrt{2}}{2}\kappa x_1\right) \sin\left(\frac{\sqrt{2}}{2}\kappa x_2\right), \quad (x_1, x_2) \in [0, 1] \times [0, 1], \quad (16)$$

which becomes increasingly oscillatory behavior as the wavenumber  $\kappa$  grows.

We first solve equation (15) with the exact solution (16) at wavenumber  $\kappa = (50, 100, 150, 200)$  by FD-MGDL and six competing methods including FD-SGDL, Mscale, FBPINN, SIREN, PINN and Pre-PINN. For all the methods except Mscale, we set  $m = (300, 500, 700, 700)$  for the respective wavenumbers and partition the interval  $[0, 1]$  into  $m + 1$  equally spaced subintervals with points

$$0 = x_{0,i} < x_{1,i} < \dots < x_{m,i} < x_{m+1,i} = 1, \quad i = 1, 2,$$

where  $x_{j,i} := jh$  and  $h := 1/(m + 1)$ . The corresponding training points are chosen as the tensor-product grid  $(x_{j_1,1}, x_{j_2,2})$ ,  $j_1, j_2 \in \mathbb{N}_m$ . For Mscale, to ensure a fair comparison in terms of training data size, the total number of training points is set to be equal to that used by the above uniform-grid-based methods divided by the number of scales. These points are then randomly sampled from the computational domain. In a similar manner, for all methods the testing points are selected as  $(\tilde{x}_{j_1,1}, \tilde{x}_{j_2,2})$ ,  $j_1, j_2 \in \mathbb{N}_{\tilde{m}}$  with  $\tilde{m} = (150, 250, 350, 350)$  corresponding to the four wavenumbers.

Table 2 presents a quantitative comparison between FD-MGDL and six baseline methods for the Helmholtz problem (15) with the exact solution (16) at wavenumber  $\kappa = 50, 100, 150, 200$ . The reported metrics include the number of training epochs, AC time, TrRSE and TeRSE. These indicators enable a comprehensive evaluation of each method in terms of accuracy, generalization, and computational efficiency.

Table 2 clearly shows that FD-MGDL outperforms all competing methods in solution accuracy. For example, at  $\kappa = 50$ , FD-MGDL attains TrRSE and TeRSE values of  $5.37 \times 10^{-4}$ , more than one order of magnitude smaller than FD-SGDL ( $\sim 10^{-3}$ ) and at least two orders of magnitude smaller than Mscale, FBPINN, and SIREN ( $\sim 10^{-2}$ ). The close agreement between training and testing errors further demonstrates excellent generalization and numerical stability, with no evidence of overfitting or spurious oscillations.

FD-MGDL also exhibits clear computational advantages. It converges within 12,400 epochs using only 6,272 seconds—substantially less than all other neural-network-based solvers. In contrast, FD-SGDL requires nearly an order of magnitude more time (49,990 seconds) despite lower accuracy, highlighting the efficiency of the multi-grade strategy. PINN and Pre-PINN fail to produce meaningful solutions (TrRSE = TeRSE = 1.00) while incurring the longest runtimes, confirming their difficulty in handling oscillatory Helmholtz problems even at moderate wavenumbers.

Among the remaining baselines, Mscale and FBPINN yield modest improvements over standard PINN but remain one to two orders of magnitude less accurate than FD-MGDL. SIREN, despite its oscillation-aware activations, still incurs large errors and high computational cost, indicating that expressive activations alone are insufficient without a hierarchical training mechanism.

The convergence behavior in Fig. 2 further supports these findings. FD-MGDL shows the fastest and most stable loss decay, reaching a low-error plateau well before all the baselines. FD-SGDL converges more

Table 2: Performance comparison of FD-MGDL, FD-SGDL, FBPINN, SIREN, PINN and Pre-PINN for the 2D Helmholtz problem (15) with the exact solution (16).

$\kappa$	Method	Epochs	AC time (s)	TrRSE	TeRSE
50	FD-MGDL	12,400	6,272	$5.37 \times 10^{-4}$	$5.37 \times 10^{-4}$
	FD-SGDL	15,000	49,990	$1.76 \times 10^{-3}$	$1.90 \times 10^{-3}$
	Mscale	15,000	9,277	$2.14 \times 10^{-2}$	$2.09 \times 10^{-2}$
	FBPINN	15,000	11,173	$1.19 \times 10^{-2}$	$1.20 \times 10^{-2}$
	SIREN	15,000	32,944	$3.06 \times 10^{-2}$	$3.08 \times 10^{-2}$
	PINN	15,000	41,431	$1.00 \times 10^0$	$1.00 \times 10^0$
	Pre-PINN	15,000	61,286	$1.00 \times 10^0$	$1.00 \times 10^0$
100	FD-MGDL	6,500	9,196	$5.54 \times 10^{-3}$	$5.56 \times 10^{-3}$
	FD-SGDL	8,000	53,636	$1.65 \times 10^{-2}$	$1.87 \times 10^{-2}$
	Mscale	8,000	13,224	$2.44 \times 10^{-2}$	$2.44 \times 10^{-2}$
	FBPINN	8,000	12,965	$4.33 \times 10^{-2}$	$4.33 \times 10^{-2}$
	SIREN	8,000	32,737	$9.96 \times 10^{-2}$	$1.00 \times 10^{-1}$
	PINN	8,000	47,792	$1.00 \times 10^0$	$1.00 \times 10^0$
	Pre-PINN	8,000	70,695	$1.00 \times 10^0$	$1.00 \times 10^0$
150	FD-MGDL	8,000	21,861	$1.31 \times 10^{-2}$	$1.34 \times 10^{-2}$
	FD-SGDL	10,000	131,216	$5.22 \times 10^{-1}$	$5.23 \times 10^{-1}$
	Mscale	10,000	33,191	$6.02 \times 10^{-2}$	$6.01 \times 10^{-2}$
	FBPINN	10,000	26,827	$6.28 \times 10^{-2}$	$6.29 \times 10^{-2}$
	SIREN	10,000	98,435	$1.06 \times 10^{-1}$	$1.06 \times 10^{-1}$
	PINN	10,000	108,747	$1.00 \times 10^0$	$1.00 \times 10^0$
	Pre-PINN	10,000	160,863	$1.00 \times 10^0$	$1.00 \times 10^0$
200	FD-MGDL	6,500	17,776	$3.92 \times 10^{-1}$	$3.92 \times 10^{-1}$
	FD-SGDL	8,000	106,135	$8.79 \times 10^{-1}$	$8.79 \times 10^{-1}$
	Mscale	8,000	23,479	$4.75 \times 10^{-1}$	$4.75 \times 10^{-1}$
	FBPINN	8,000	26,827	$8.22 \times 10^{-1}$	$8.22 \times 10^{-1}$
	SIREN	8,000	63,123	$8.95 \times 10^{-1}$	$8.98 \times 10^{-1}$
	PINN	8,000	88,110	$1.00 \times 10^0$	$1.00 \times 10^0$
	Pre-PINN	8,000	139,890	$1.00 \times 10^0$	$1.00 \times 10^0$

slowly and stagnates at a higher level, while other methods exhibit slow or unstable optimization, consistent with Table 2. These results confirm that multi-grade learning effectively mitigates the optimization challenges posed by highly oscillatory solutions.

Figures 2 (b)–(i) compare the exact solution with the error distributions of the numerical methods. FD-MGDL produces a uniformly small and well-structured error field without spurious oscillations, accurately capturing both amplitude and phase. In contrast, FD-SGDL shows noticeable residual errors, while Mscale, FBPINN, and SIREN exhibit substantially larger and spatially irregular errors. PINN and Pre-PINN are dominated by large-scale discrepancies, confirming their inability to resolve the oscillatory solution even at this moderate wavenumber.

The same trends persist for higher wavenumbers. Figures 3–5 show that as  $\kappa$  increases and the solution becomes more oscillatory, all baseline methods suffer from deteriorating convergence and rapidly growing errors, whereas FD-MGDL maintains stable training and well-controlled error distributions. The loss curves in Figs. 3–5 (a) further indicate that FD-MGDL remains robust to increasing frequency content, while the baselines exhibit stagnation or divergence.

Overall, Table 2 and Figs. 2–5 confirm that FD-MGDL achieves a superior balance of accuracy, robustness, and efficiency across a wide range of wavenumbers. The multi-grade strategy effectively mitigates spectral bias and optimization difficulties inherent in standard PINN-type methods, enabling reliable solution of high-frequency Helmholtz problems.

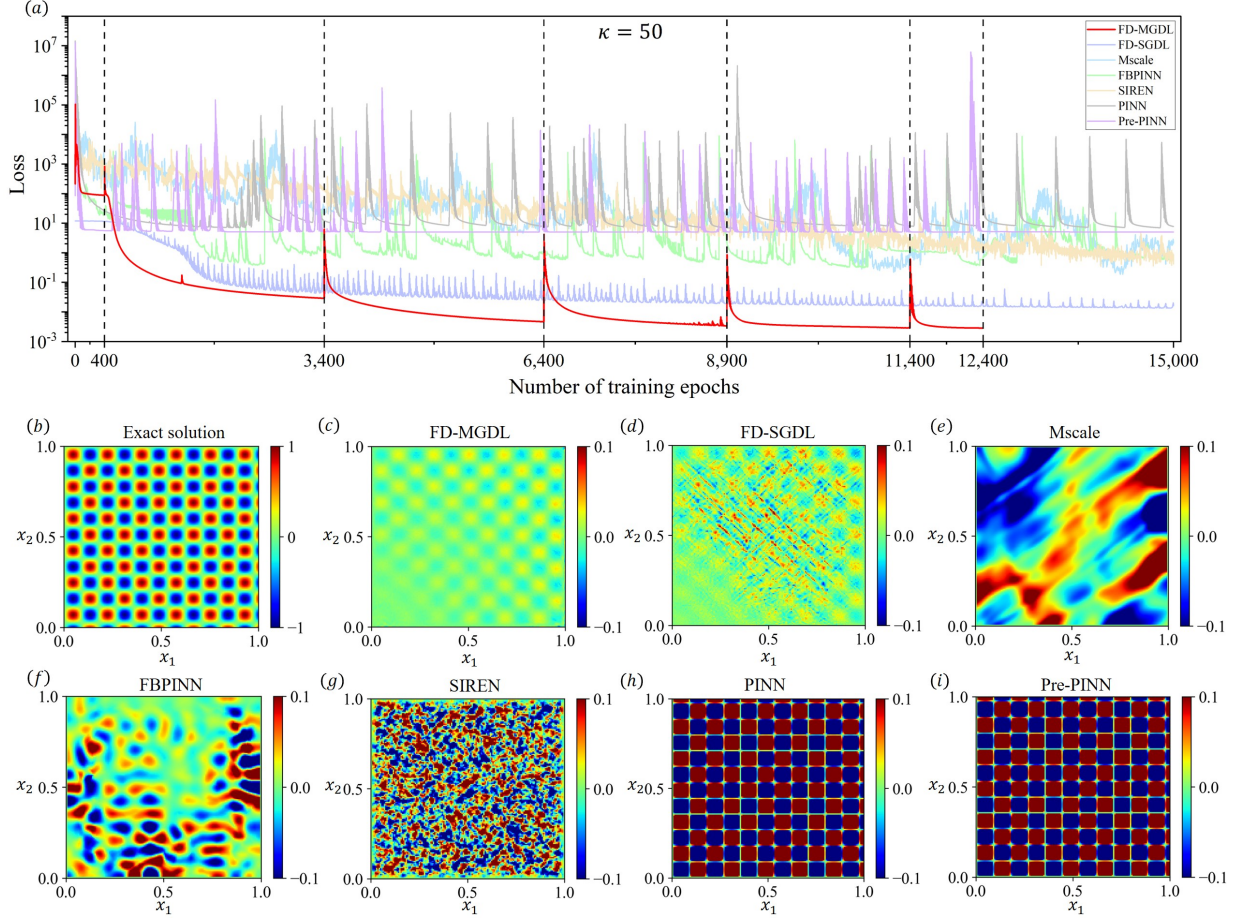


Figure 2: Performance comparison of FD-MGDL and six baseline methods (FD-SGDL, Mscale, FBPINN, SIREN, PINN and Pre-PINN) for the 2D Helmholtz problem (15) with the exact solution (16) at  $\kappa = 50$ : (a) training loss curves; (b) exact solution; (c) – (i) error visualizations of the numerical solutions.

## 5.2 Plane Wave Propagation Problem

We next consider a two-dimensional Helmholtz problem with a plane wave solution to further assess the performance of different numerical methods in the high-wavenumber regime. Owing to the unsatisfactory performance of the baseline PINN, SIREN, and Pre-PINN methods observed in the first experiment, we restrict the subsequent comparative analysis to the FD-MGDL, FD-SGDL, Mscale, and FBPINN approaches in this and the following experiments.

In this test case, we consider a homogeneous source term,  $f(\mathbf{x}) = 0$ , on the unit square  $\Omega := (0, 1)^2$ . Dirichlet boundary conditions are prescribed on  $\partial\Omega := \bigcup_{j=1}^4 \Gamma_j$  such that the boundary data  $g$  is consistent with the exact monochromatic plane-wave solution:

$$u(x_1, x_2) = \exp[i(\kappa_1 x_1 + \kappa_2 x_2)], \quad \mathbf{x} \in \bar{\Omega}, \quad (17)$$

where the wave vector components are  $(\kappa_1, \kappa_2) := \kappa(\cos\theta, \sin\theta)$ , with  $\kappa$  denoting the wavenumber and  $\theta \in [0, 2\pi)$  the propagation angle.

Specifically, the boundary function  $g$  is defined piecewise:

$$g(x_1, x_2) = \begin{cases} \exp(i\kappa_2 x_2), & \text{on } \Gamma_1 := 0 \times (0, 1); \\ \exp(i\kappa_1 x_1), & \text{on } \Gamma_2 := (0, 1) \times 0; \\ \exp[i(\kappa_1 + \kappa_2 x_2)], & \text{on } \Gamma_3 := 1 \times (0, 1); \\ \exp[i(\kappa_1 x_1 + \kappa_2)], & \text{on } \Gamma_4 := (0, 1) \times 1. \end{cases}$$

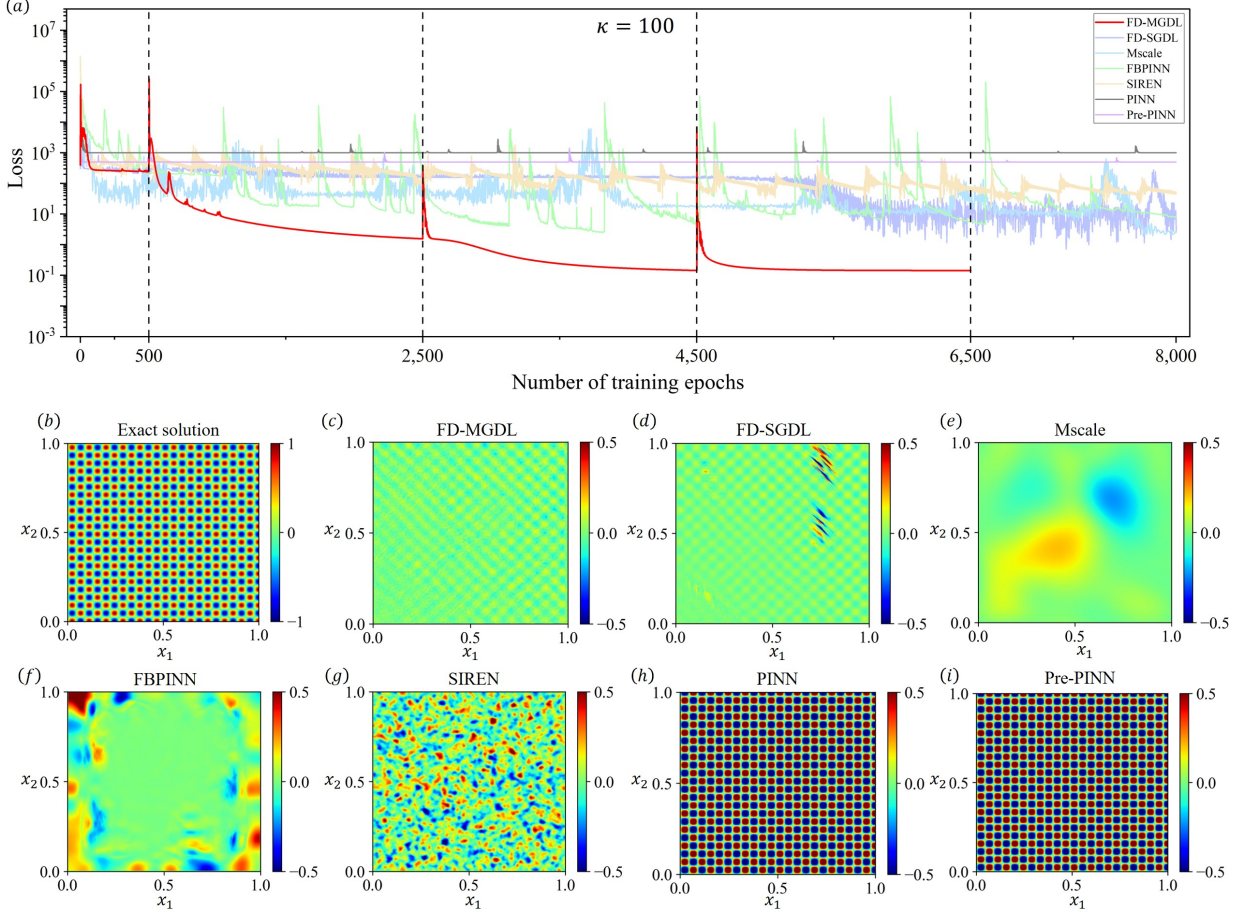


Figure 3: Performance comparison of FD-MGDL and six baseline methods (FD-SGDL, Mscale, FBPINN, SIREN, PINN and Pre-PINN) for the 2D Helmholtz problem (15) with the exact solution (16) at  $\kappa = 100$ : (a) training loss curves; (b) exact solution; (c) – (i) error visualizations of the numerical solutions.

As the wavenumber  $\kappa$  increases, the solution becomes highly oscillatory, posing a significant challenge for numerical approximation methods due to the stringent sampling requirements needed to resolve the wave phases.

We evaluate the performance of FD-MGDL, FD-SGDL, Mscale, and FBPINN for  $\kappa \in \{50, 100, 150, 200\}$  and a fixed direction  $\theta = \pi/4$ . To resolve the increasing oscillations, we scale the number of grid points  $m$  with  $\kappa$ , setting  $m \in \{300, 500, 700, 700\}$  for training and  $\bar{m} \in \{150, 250, 350, 350\}$  for testing. Training points for most methods are arranged on a tensor-product grid; however, for Mscale, points are randomly sampled to maintain a total count equivalent to the other methods divided by the number of scales.

Table 3 summarizes the performance of FD-MGDL alongside three baselines — FD-SGDL, Mscale, and FBPINN — for wavenumbers  $\kappa \in \{50, 100, 150, 200\}$ . Across all cases, FD-MGDL demonstrates superior accuracy and efficiency. At  $\kappa = 50$ , it achieves training (TrRSE) and testing (TeRSE) errors on the order of  $10^{-4}$  with significantly fewer epochs and lower computational cost than FD-SGDL. In contrast, Mscale and FBPINN yield errors one to two orders of magnitude higher, struggling to resolve the plane wave structure.

As  $\kappa$  increases, the intensified oscillations exacerbate numerical difficulty. While all baseline methods experience rapid accuracy degradation, FD-MGDL consistently maintains the lowest error levels. For  $\kappa = 100$  and 150, its relative errors remain roughly an order of magnitude smaller than those of Mscale and FBPINN, and several orders smaller than FD-SGDL. Even at the extreme  $\kappa = 200$ , FD-MGDL remains the most robust, whereas baselines suffer from pronounced error growth typically associated with pollution effects and optimization stagnation.

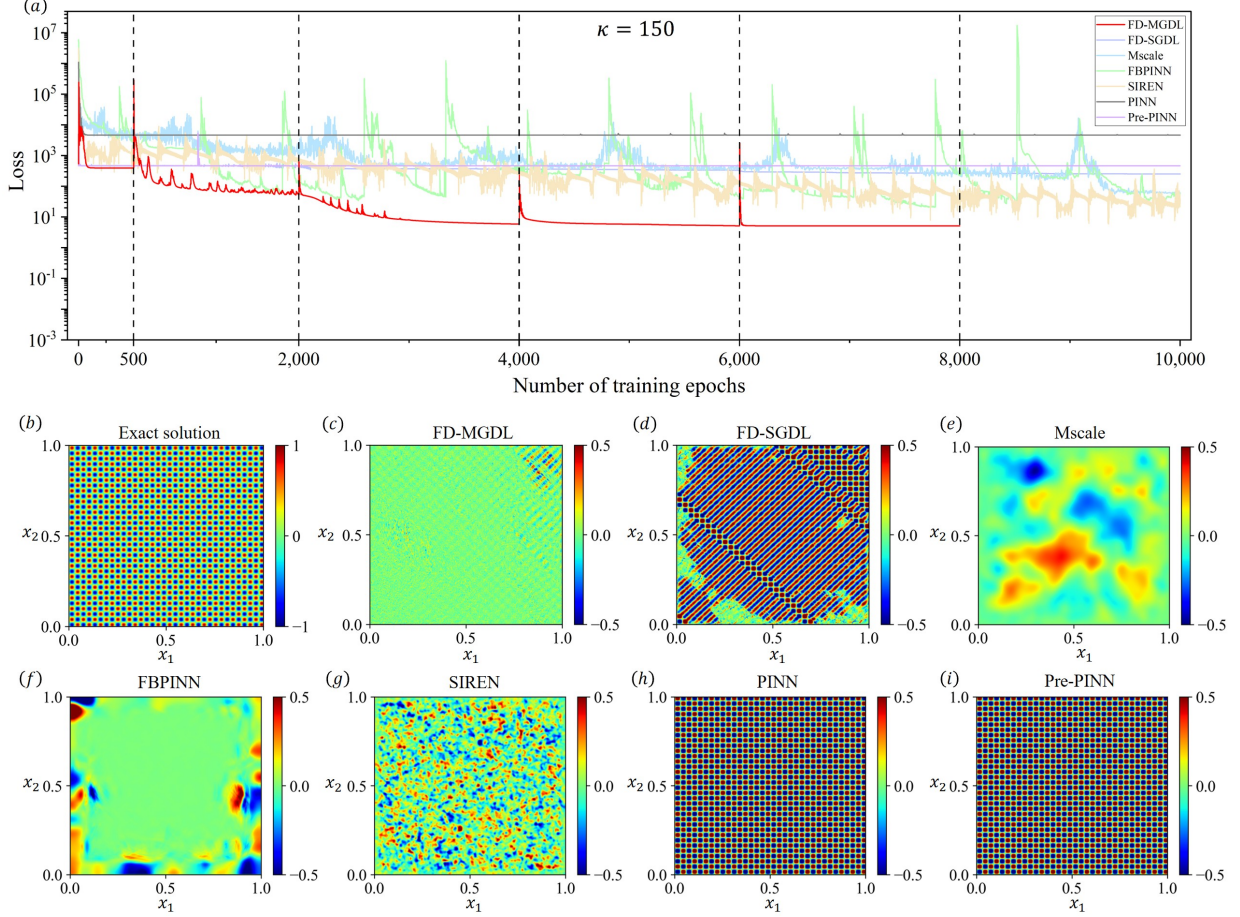


Figure 4: Performance comparison of FD-MGDL and six baseline methods (FD-SGDL, Mscale, FBPINN, SIREN, PINN and Pre-PINN) for the 2D Helmholtz problem (15) with the exact solution (16) at  $\kappa = 150$ : (a) training loss curves; (b) exact solution; (c) – (i) error visualizations of the numerical solutions.

Convergence dynamics are further illustrated in Figure 6. FD-MGDL exhibits faster and more stable loss decay across the entire wavenumber spectrum. Conversely, FD-SGDL stagnates prematurely, and both Mscale and FBPINN display increasingly erratic trajectories as the frequency rises.

In summary, these experiments confirm that FD-MGDL achieves high precision at moderate wavenumbers and exceptional robustness in high-frequency regimes. By effectively mitigating the convergence hurdles and accuracy loss observed in existing PINN and multiscale solvers, the multigrade learning strategy establishes FD-MGDL as a highly reliable approach for oscillatory Helmholtz problems.

## 6 Three-dimensional Helmholtz equations

In this section, we consider the three-dimensional Helmholtz equation with Dirichlet boundary conditions:

$$\begin{cases} \frac{\partial^2 u}{\partial x_1^2} + \frac{\partial^2 u}{\partial x_2^2} + \frac{\partial^2 u}{\partial x_3^2} + \kappa^2 u(x_1, x_2, x_3) = f(x_1, x_2, x_3), & (x_1, x_2, x_3) \in \Omega, \\ u(x_1, x_2, x_3) = g(x_1, x_2, x_3), & (x_1, x_2, x_3) \in \Gamma. \end{cases} \quad (18)$$

We compare the performance of FD-MGDL, FD-SGDL, Mscale and FBPINN for solving equation (18) in the large-wavenumbers regime.

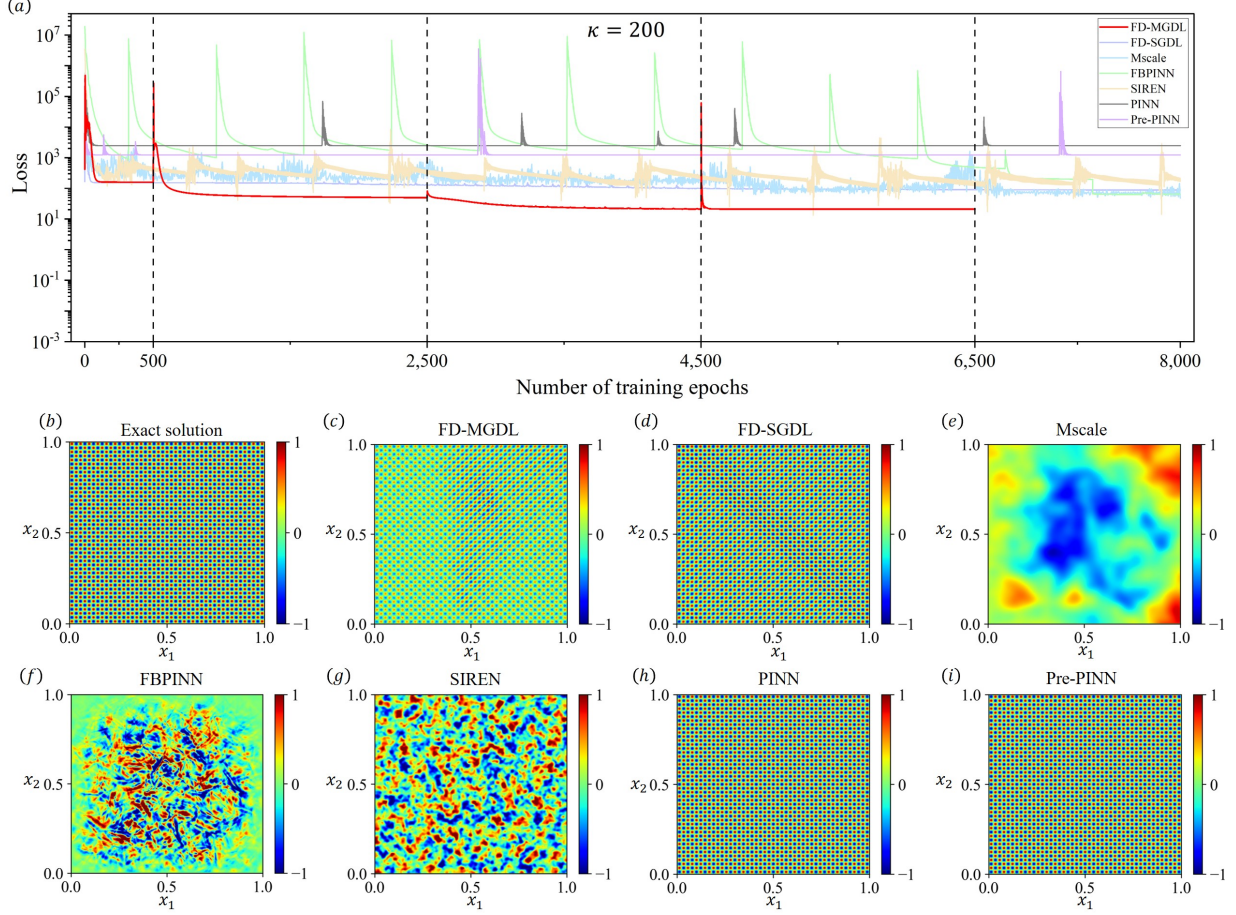


Figure 5: Performance comparison of FD-MGDL and six baseline methods (FD-SGDL, Mscale, FBPINN, SIREN, PINN and Pre-PINN) for the 2D Helmholtz problem (15) with the exact solution (16) at  $\kappa = 200$ : (a) training loss curves; (b) exact solution; (c) – (i) error visualizations of the numerical solutions.

## 6.1 Highly Oscillatory Sine Solution

We evaluate the performance of the proposed method against several baselines using a test case of (18) with a highly oscillatory sinusoidal solution; this facilitates a comparative analysis of the methods' efficacy in the high-wavenumber regime.

In this test case, we consider a homogeneous source term,  $f(\mathbf{x}) = 0$ , over the unit cubic domain  $\Omega = (0, 1)^3$ . Dirichlet boundary conditions are prescribed on  $\partial\Omega := \bigcup_{i=1}^6 \Gamma_i$  as follows:

$$g(x_1, x_2, x_3) = \begin{cases} 0, & \text{if } (x_1, x_2, x_3) \in \Gamma_1 := \{0\} \times (0, 1) \times (0, 1); \\ 0, & \text{if } (x_1, x_2, x_3) \in \Gamma_2 := (0, 1) \times \{0\} \times (0, 1); \\ 0, & \text{if } (x_1, x_2, x_3) \in \Gamma_3 := (0, 1) \times (0, 1) \times \{0\}; \\ \sin\left(\frac{\sqrt{3}}{3}\kappa\right) \sin\left(\frac{\sqrt{3}}{3}\kappa x_2\right) \sin\left(\frac{\sqrt{3}}{3}\kappa x_3\right), & \text{if } (x_1, x_2, x_3) \in \Gamma_4 := \{1\} \times (0, 1) \times (0, 1); \\ \sin\left(\frac{\sqrt{3}}{3}\kappa x_1\right) \sin\left(\frac{\sqrt{3}}{3}\kappa\right) \sin\left(\frac{\sqrt{3}}{3}\kappa x_3\right), & \text{if } (x_1, x_2, x_3) \in \Gamma_5 := (0, 1) \times \{1\} \times (0, 1); \\ \sin\left(\frac{\sqrt{3}}{3}\kappa x_1\right) \sin\left(\frac{\sqrt{3}}{3}\kappa x_2\right) \sin\left(\frac{\sqrt{3}}{3}\kappa\right), & \text{if } (x_1, x_2, x_3) \in \Gamma_6 := (0, 1) \times (0, 1) \times \{1\}, \end{cases}$$

where  $\kappa$  is a constant wavenumber. Under these conditions, the analytical solution to (18) is:

$$u(x_1, x_2, x_3) = \sin\left(\frac{\sqrt{3}}{3}\kappa x_1\right) \sin\left(\frac{\sqrt{3}}{3}\kappa x_2\right) \sin\left(\frac{\sqrt{3}}{3}\kappa x_3\right), \quad (x_1, x_2, x_3) \in [0, 1] \times [0, 1] \times [0, 1], \quad (19)$$

Table 3: Performance comparison of FD-MGDL, FD-SGDL, Mscale and FBPINN for the 2D Helmholtz problem (15) with the exact solution (17).

$\kappa$	Method	Epoch	AC time (s)	TrRSE	TeRSE
50	FD-MGDL	4,500	2,540	$3.40 \times 10^{-4}$	$3.42 \times 10^{-4}$
	FD-SGDL	6,000	14,079	$3.54 \times 10^{-3}$	$3.57 \times 10^{-3}$
	Mscale	6,000	2,823	$3.90 \times 10^{-2}$	$3.82 \times 10^{-2}$
	FBPINN	6,000	4,544	$1.02 \times 10^{-2}$	$1.02 \times 10^{-2}$
100	FD-MGDL	6,500	9,493	$2.82 \times 10^{-3}$	$2.83 \times 10^{-3}$
	FD-SGDL	8,000	57,681	$4.03 \times 10^{-1}$	$4.03 \times 10^{-1}$
	Mscale	8,000	11,548	$1.89 \times 10^{-2}$	$1.81 \times 10^{-2}$
	FBPINN	8,000	16,066	$5.82 \times 10^{-2}$	$5.82 \times 10^{-2}$
150	FD-MGDL	2,500	6,894	$8.07 \times 10^{-3}$	$8.07 \times 10^{-3}$
	FD-SGDL	5,000	40,342	$8.16 \times 10^{-2}$	$8.19 \times 10^{-2}$
	Mscale	5,000	13,799	$2.12 \times 10^{-1}$	$2.09 \times 10^{-1}$
	FBPINN	5,000	21,367	$1.37 \times 10^{-1}$	$1.37 \times 10^{-1}$
200	FD-MGDL	3,500	10,462	$5.20 \times 10^{-2}$	$5.21 \times 10^{-2}$
	FD-SGDL	5,000	70,964	$7.37 \times 10^{-1}$	$7.38 \times 10^{-1}$
	Mscale	5,000	14,292	$2.79 \times 10^{-1}$	$2.74 \times 10^{-1}$
	FBPINN	5,000	20,103	$2.65 \times 10^{-1}$	$2.65 \times 10^{-1}$

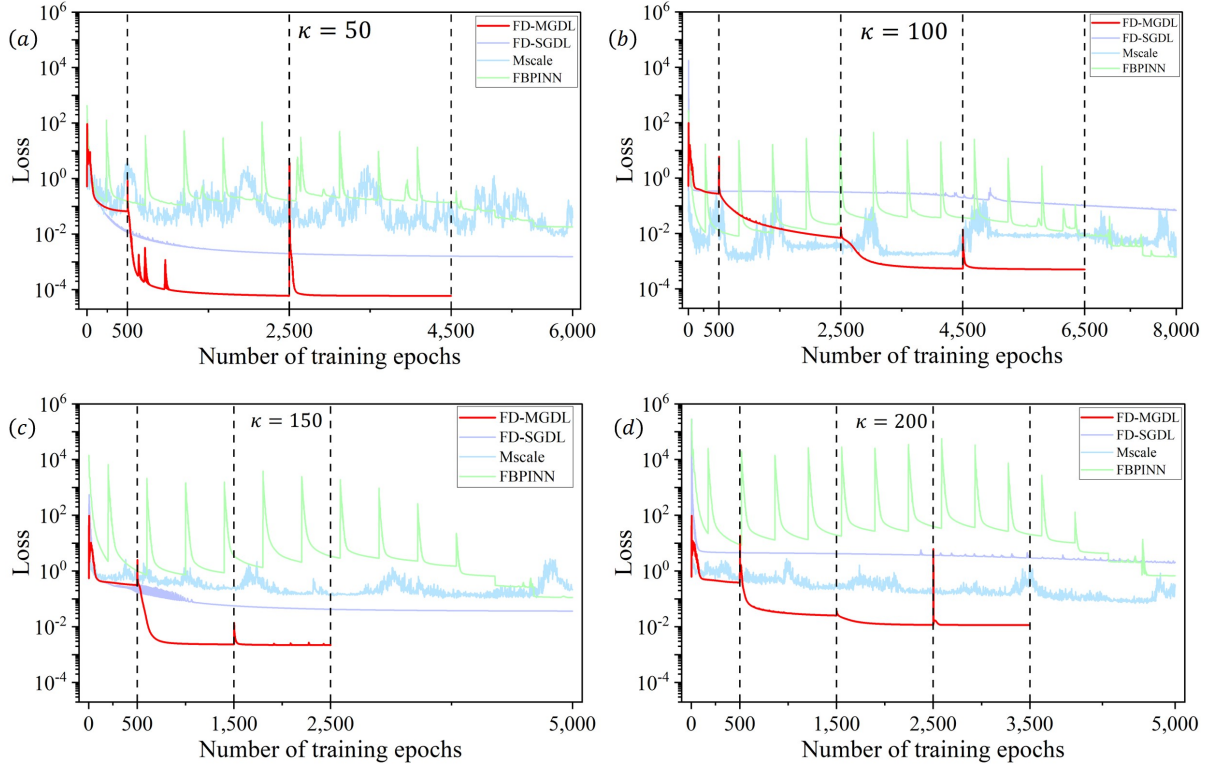


Figure 6: Performance comparison of training loss curves of FD-MGDL and three baseline methods (FD-SGDL, Mscale and FBPINN) for the 2D Helmholtz problem (15) with the exact solution (17): (a)  $\kappa = 50$ ; (b)  $\kappa = 100$ ; (c)  $\kappa = 150$ ; (d)  $\kappa = 200$ .

which exhibits increasingly rapid oscillations as  $\kappa$  increases. This test case is specifically designed to ensure that the exact solution possesses a uniform degree of oscillation across all three coordinate directions, directly proportional to  $\kappa$ .

We solve the equation (18) with the exact solution (19) for wavenumbers  $\kappa \in \{20, 30, 40, 50\}$  utilizing FD-MGDL, FD-SGDL, Mscale, and FBPINN. For all methods excluding Mscale, we set  $m = 60$  and discretize the unit interval  $[0, 1]$  into  $m + 1$  uniform subintervals. The resulting grid points are defined as  $x_{j,i} := jh$  for  $j \in \{0, \dots, m + 1\}$  and  $i \in \{1, 2, 3\}$ , with a mesh size of  $h := 1/(m + 1)$ . The training set is constructed using a tensor-product grid of these points:  $\mathcal{X}_{train} = \{(x_{j_1,1}, x_{j_2,2}, x_{j_3,3}) : j_1, j_2, j_3 \in \mathbb{N}_m\}$ . For the Mscale method, training points are randomly sampled from the computational domain  $\Omega$ ; the total number of samples is kept consistent with the other methods by dividing the tensor-grid cardinality by the number of scales. For performance evaluation, testing points  $\{(\tilde{x}_{j_1,1}, \tilde{x}_{j_2,2}, \tilde{x}_{j_3,3}) : j_1, j_2, j_3 \in \mathbb{N}_{\tilde{m}}\}$  are generated similarly using  $\tilde{m} = 30$  for all models.

Table 4: Performance comparison of FD-MGDL, FD-SGDL, Mscale and FBPINN for the 3D Helmholtz problem (18) with the exact solution (19).

$\kappa$	Method	Epoch	AC time (s)	TrRSE	TeRSE
20	FD-MGDL	8,500	10,828	$2.74 \times 10^{-2}$	$3.31 \times 10^{-2}$
	FD-SGDL	10,000	77,071	$2.93 \times 10^{-2}$	$3.55 \times 10^{-2}$
	Mscale	10,000	20,117	$1.89 \times 10^{-1}$	$1.71 \times 10^{-1}$
	FBPINN	10,000	23,167	$1.19 \times 10^{-1}$	$1.19 \times 10^{-1}$
30	FD-MGDL	6,000	8,038	$1.69 \times 10^{-2}$	$1.81 \times 10^{-2}$
	FD-SGDL	8,000	33,722	$1.77 \times 10^{-1}$	$2.85 \times 10^{-1}$
	Mscale	8,000	16,119	$5.08 \times 10^{-1}$	$4.13 \times 10^{-1}$
	FBPINN	8,000	21,090	$2.82 \times 10^{-1}$	$2.83 \times 10^{-1}$
40	FD-MGDL	12,500	12,810	$3.13 \times 10^{-1}$	$3.28 \times 10^{-1}$
	FD-SGDL	15,000	145,043	$4.30 \times 10^{-1}$	$4.58 \times 10^{-1}$
	Mscale	15,000	29,865	$5.58 \times 10^{-1}$	$4.57 \times 10^{-1}$
	FBPINN	15,000	38,613	$7.37 \times 10^{-1}$	$7.37 \times 10^{-1}$
50	FD-MGDL	6,500	8,646	$3.48 \times 10^{-1}$	$3.91 \times 10^{-1}$
	FD-SGDL	8,000	64,206	$9.85 \times 10^{-1}$	$9.86 \times 10^{-1}$
	Mscale	8,000	14,597	$6.00 \times 10^{-1}$	$5.46 \times 10^{-1}$
	FBPINN	8,000	24,292	$9.25 \times 10^{-1}$	$9.25 \times 10^{-1}$

Table 4 presents a comparative analysis of FD-MGDL against three baselines — FD-SGDL, Mscale, and FBPINN — for wavenumbers  $\kappa \in \{20, 30, 40, 50\}$ . Moving from two to three dimensions significantly increases computational complexity and exacerbates the difficulties inherent in capturing oscillatory wave propagation.

At  $\kappa = 20$ , FD-MGDL achieves the superior performance, yielding the lowest training (TrRSE) and testing (TeRSE) errors. Notably, while FD-SGDL achieves comparable accuracy, its computational cost is nearly an order of magnitude higher, highlighting the poor scalability of single-grade networks in 3D. Meanwhile, Mscale and FBPINN exhibit markedly higher errors, struggling to resolve the 3D oscillatory structure.

As  $\kappa$  increases to 30 and 40, the problem’s numerical difficulty rises sharply, leading to a general deterioration in accuracy across all solvers. Nevertheless, FD-MGDL consistently maintains the lowest error levels with reduced computational overhead. For  $\kappa = 30$ , FD-MGDL preserves a testing error on the order of  $10^{-2}$ , whereas baseline errors escalate to  $10^{-1}$  or even  $10^0$ . This suggests that the multigrade strategy effectively mitigates optimization challenges in moderately high-frequency regimes.

At the highest wavenumber ( $\kappa = 50$ ), the severe oscillations cause substantial error growth in all methods. However, FD-MGDL remains the most robust, avoiding the near-complete loss of accuracy observed in FD-SGDL and FBPINN. Its relative performance advantage in this regime underscores the stability conferred by the multi-grade approach.

Convergence dynamics are illustrated via the training loss curves in Fig. 7. FD-MGDL displays faster and more stable decay across all wavenumbers. In contrast, FD-SGDL suffers from stagnation as  $\kappa$  increases, while Mscale and FBPINN exhibit increasingly irregular training trajectories. These qualitative observations align closely with the quantitative results in Table 4.

In summary, these 3D experiments demonstrate that FD-MGDL effectively scales to higher-dimensional

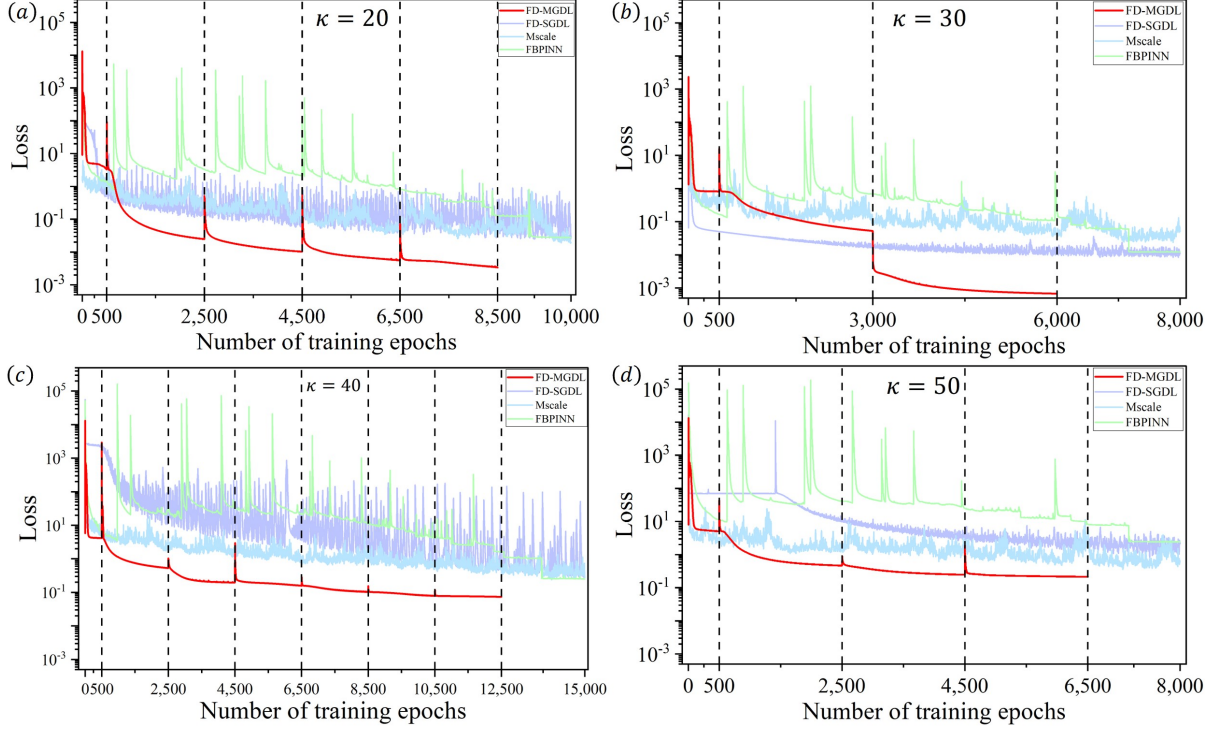


Figure 7: Performance comparison of training loss curves of FD-MGDL and three baseline methods (FD-SGDL, Mscale and FBPINN) for the 3D Helmholtz problem (18) with the exact solution (19): (a)  $\kappa = 20$ ; (b)  $\kappa = 30$ ; (c)  $\kappa = 40$ ; (d)  $\kappa = 50$ .

Helmholtz problems. It offers a superior trade-off between accuracy and efficiency, delivering more robust solutions than existing SGDL, Multiscale, and PINN-based approaches in high-frequency settings.

## 6.2 Plane Wave Propagation Problem

We extend the plane wave benchmark from subsection 5.2 to the three-dimensional unit cube  $\Omega = (0, 1)^3$ , assessing the numerical methods in higher-dimensional, high-wavenumber regimes.

For this test case, we consider the homogeneous Helmholtz equation ( $f = 0$ ). Dirichlet boundary conditions are prescribed on  $\partial\Omega = \bigcup_{j=1}^6 \Gamma_j$ , with the boundary data  $g$  consistent with the exact solution:

$$u(x_1, x_2, x_3) = \exp[i(\kappa_1 x_1 + \kappa_2 x_2 + \kappa_3 x_3)], \quad \mathbf{x} \in \bar{\Omega}. \quad (20)$$

The wave vector components are defined as  $(\kappa_1, \kappa_2, \kappa_3) := \kappa(\cos \phi \cos \theta, \cos \phi \sin \theta, \sin \phi)$ , where  $\kappa$  is the wavenumber and  $(\phi, \theta)$  are the angular parameters determining the propagation direction. Specifically, the boundary function  $g$  is given by:

$$g(x_1, x_2, x_3) = \begin{cases} \exp[i(\kappa_2 x_2 + \kappa_3 x_3)], & \text{if } (x_1, x_2, x_3) \in \Gamma_1 := \{0\} \times (0, 1)^2; \\ \exp[i(\kappa_1 x_1 + \kappa_3 x_3)], & \text{if } (x_1, x_2, x_3) \in \Gamma_2 := (0, 1) \times \{0\} \times (0, 1); \\ \exp[i(\kappa_1 x_1 + \kappa_2 x_2)], & \text{if } (x_1, x_2, x_3) \in \Gamma_3 := (0, 1)^2 \times \{0\}; \\ \exp[i(\kappa_1 + \kappa_2 x_2 + \kappa_3 x_3)], & \text{if } (x_1, x_2, x_3) \in \Gamma_4 := \{1\} \times (0, 1)^2; \\ \exp[i(\kappa_1 x_1 + \kappa_2 + \kappa_3 x_3)], & \text{if } (x_1, x_2, x_3) \in \Gamma_5 := (0, 1) \times \{1\} \times (0, 1); \\ \exp[i(\kappa_1 x_1 + \kappa_2 x_2 + \kappa_3)], & \text{if } (x_1, x_2, x_3) \in \Gamma_6 := (0, 1)^2 \times \{1\}. \end{cases}$$

This setup represents a monochromatic plane wave whose oscillations intensify as  $\kappa$  increases. Resolving such high-frequency wave fields in 3D remains a significant numerical challenge, particularly regarding the trade-off between discretization density and computational efficiency.

We solve the homogeneous Helmholtz equation to approximate the exact plane-wave solution (20) for wavenumbers  $\kappa \in \{20, 30\}$  with propagation angles  $\phi = \pi/3$  and  $\theta = \pi/8$ . We compare the performance of FD-MGDL, FD-SGDL, Mscale, and FBPINN. Following the setup in the previous experiment, training points for most methods are defined on a tensor-product grid with  $m = 60$ , while testing points are defined similarly with  $\tilde{m} = 30$ . For the Mscale method, training points are randomly sampled from the domain  $\Omega$ , maintaining a total sample count equivalent to the other methods divided by the number of scales.

Table 5: Performance comparison of FD-MGDL, FD-SGDL, Mscale and FBPINN for the 3D Helmholtz problem (18) with the exact solution (20).

$\kappa$	Method	Epoch	AC time (s)	TrRSE	TeRSE
20	FD-MGDL	3,500	5,200	$4.16 \times 10^{-2}$	$4.29 \times 10^{-2}$
	FD-SGDL	5,000	41,358	$7.69 \times 10^{-1}$	$7.79 \times 10^{-1}$
	Mscale	5,000	9,142	$3.18 \times 10^{-1}$	$2.70 \times 10^{-1}$
	FBPINN	5,000	12,950	$3.04 \times 10^{-1}$	$3.04 \times 10^{-1}$
30	FD-MGDL	3,500	4,998	$2.51 \times 10^{-1}$	$2.59 \times 10^{-1}$
	FD-SGDL	5,000	40,978	$9.19 \times 10^{-1}$	$9.28 \times 10^{-1}$
	Mscale	5,000	9,051	$6.66 \times 10^{-1}$	$5.91 \times 10^{-1}$
	FBPINN	5,000	12,881	$7.28 \times 10^{-1}$	$7.28 \times 10^{-1}$

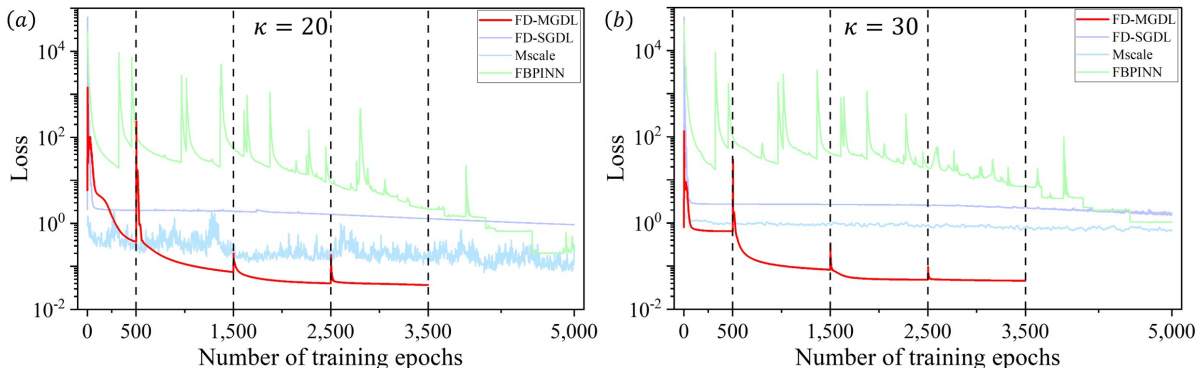


Figure 8: Performance comparison of training loss curves of FD-MGDL and three baseline methods (FD-SGDL, Mscale and FBPINN) for the 3D Helmholtz problem (18) with the exact solution (20): (a)  $\kappa = 20$ ; (b)  $\kappa = 30$ .

Table 5 presents a quantitative comparison of FD-MGDL with FD-SGDL, Mscale, and FBPINN for wavenumbers  $\kappa = 20$  and 30. Compared with the three-dimensional sinusoidal solution, the plane wave configuration places stronger emphasis on accurate phase propagation and directional consistency, thereby posing additional challenges for neural-network-based solvers.

For  $\kappa = 20$ , FD-MGDL achieves the highest accuracy among all tested methods, with TrRSE and TeRSE values on the order of  $10^{-2}$ , while requiring substantially fewer training epochs and significantly lower accumulated computational time. In contrast, FD-SGDL exhibits severe accuracy degradation, with relative errors approaching unity despite its markedly higher computational cost. Mscale and FBPINN improve upon FD-SGDL in terms of efficiency, yet their error levels remain an order of magnitude larger than those of FD-MGDL, indicating insufficient phase accuracy even at this moderate wavenumber.

As the wavenumber increases to  $\kappa = 30$ , the limitations of the baseline methods become even more pronounced. Table 5 shows that FD-SGDL, Mscale, and FBPINN all suffer from substantial error growth, with TrRSE and TeRSE values ranging from  $\mathcal{O}(10^{-1})$  to  $\mathcal{O}(10^0)$ . In contrast, FD-MGDL maintains a clear accuracy advantage, yielding the smallest errors and converging with only 4,998 seconds. Although the absolute error level increases compared with the lower-wavenumber case, FD-MGDL remains the most reliable solver among the tested approaches.

The convergence characteristics are further illustrated in Fig. 8, which displays the training loss curves

for  $\kappa = 20$  and  $30$ . As shown in Fig. 8 (a)–(b), FD-MGDL consistently demonstrates faster and smoother loss decay, whereas the baseline methods exhibit slow convergence and early stagnation. These trends are consistent with the quantitative results in Table 5 and highlight the effectiveness of the multigrade learning strategy in alleviating optimization difficulties associated with three-dimensional oscillatory wave propagation.

In summary, the three-dimensional plane wave experiments confirm that FD-MGDL extends robustly to high-dimensional, phase-sensitive Helmholtz problems. By achieving a favorable balance between accuracy and computational efficiency, FD-MGDL substantially outperforms existing SGDL, Multiscale and PINN-based solvers, further demonstrating its potential for practical three-dimensional wave simulations.

## 7 Comparison with Finite Difference Method

In this section, we evaluate FD-MGDL against the traditional Finite Difference Method (FDM), a widely used numerical baseline for Helmholtz equations on structured grids [39, 40, 41].

### 7.1 Methodology and Interpolation

The FDM solution is computed on the structured grid defined by the training points

$$\mathcal{X}_{train} = \{(x_{j_1,1}, \dots, x_{j_d,d}) : j_i \in \mathbb{N}_m, i \in \mathbb{N}_d\}.$$

We employ a standard second-order central difference stencil to discretize the Laplacian operator, solving the resulting sparse linear system to obtain nodal values.

Because the testing points

$$\mathcal{X}_{test} = \{(\tilde{x}_{j_1,1}, \dots, \tilde{x}_{j_d,d}) : j_i \in \mathbb{N}_{\tilde{m}}, i \in \mathbb{N}_d\}$$

generally do not coincide with the grid nodes, off-grid values must be estimated. To rigorously evaluate FDM performance under varying post-processing accuracies, we implement both linear and quadratic interpolation schemes.

Consider a testing point  $\tilde{\mathbf{x}} = (\tilde{x}_1, \tilde{x}_2, \dots, \tilde{x}_d)$  located in the grid cell

$$\Omega_{\mathbf{j}} = \prod_{i=1}^d [x_{j_i,1}, x_{j_i+1,1}], \quad \mathbf{j} = (j_i : i \in \mathbb{N}_d),$$

defined by the training grid. We define local normalized coordinates  $\xi_i = (\tilde{x}_i - x_{j_i,i})/h$  for  $i \in \mathbb{N}_d$ , such that  $\boldsymbol{\xi} = (\xi_1, \xi_2, \dots, \xi_d) \in [0, 1]^d$ . The interpolation schemes are defined as follows:

1. **Linear interpolation:** The predicted value  $\tilde{u}_{test}$  at the testing point  $\tilde{\mathbf{x}}$  is computed as a multilinear combination of the nodal values at the  $2^d$  vertices of the cell  $\Omega_{\mathbf{j}}$ :

$$\tilde{u}_{test} = \sum_{\boldsymbol{\alpha} \in \{0,1\}^d} \left( \prod_{i=1}^d [\alpha_i \xi_i + (1 - \alpha_i)(1 - \xi_i)] \right) \tilde{u}_{\mathbf{j}+\boldsymbol{\alpha}},$$

where  $\tilde{u}_{\mathbf{j}+\boldsymbol{\alpha}}$  is the FDM solution at the grid node  $(x_{j_1+\alpha_1,1}, \dots, x_{j_d+\alpha_d,d})$ .

2. **Quadratic interpolation:** To achieve higher-order post-processing accuracy,  $\tilde{u}_{test}$  is reconstructed using the tensor product of one-dimensional quadratic Lagrange polynomials:

$$\tilde{u}_{test} = \sum_{\mathbf{p} \in \{0,1,2\}^d} \left( \prod_{i=1}^d \mathcal{L}_{p_i}(\xi_i) \right) \tilde{u}_{\mathbf{j}+\mathbf{p}},$$

where  $\mathbf{p} = (p_1, \dots, p_d)$  indices the local  $3^d$  nodes. The basis functions  $\mathcal{L}_k(\xi)$  are defined on the reference nodes  $\{\xi_0 = 0, \xi_1 = 1/2, \xi_2 = 1\}$  as:

$$\mathcal{L}_k(\xi) = \prod_{\substack{r=0 \\ r \neq k}}^2 \frac{\xi - \xi_r}{\xi_k - \xi_r}.$$

Table 6: Performance comparison of FDM and FD-MGDL for the 2D Helmholtz problem (15) with the exact solution (16).

$\kappa$	Method	TrRSE	TeRSE	
			Bilinear	Biquadratic
50	FDM	$5.48 \times 10^{-4}$	$8.84 \times 10^{-3}$	$8.80 \times 10^{-3}$
	FD-MGDL	$5.37 \times 10^{-4}$	$5.37 \times 10^{-4}$	
100	FDM	$2.69 \times 10^{-1}$	$2.71 \times 10^{-1}$	$2.71 \times 10^{-1}$
	FD-MGDL	$5.54 \times 10^{-3}$	$5.56 \times 10^{-3}$	
150	FDM	$2.03 \times 10^{-2}$	$2.54 \times 10^{-2}$	$2.63 \times 10^{-2}$
	FD-MGDL	$1.31 \times 10^{-2}$	$1.34 \times 10^{-2}$	
200	FDM	$6.88 \times 10^{-1}$	$6.88 \times 10^{-1}$	$6.86 \times 10^{-1}$
	FD-MGDL	$3.92 \times 10^{-1}$	$3.92 \times 10^{-1}$	

Table 7: Performance comparison of FDM and FD-MGDL for the 2D Helmholtz problem (15) with the exact solution (17).

$\kappa$	Method	TrRSE	TeRSE	
			Bilinear	Biquadratic
50	FDM	$4.25 \times 10^{-4}$	$4.24 \times 10^{-4}$	$4.22 \times 10^{-4}$
	FD-MGDL	$3.40 \times 10^{-4}$	$3.42 \times 10^{-4}$	
100	FDM	$2.61 \times 10^{-1}$	$2.60 \times 10^{-1}$	$2.60 \times 10^{-1}$
	FD-MGDL	$2.82 \times 10^{-3}$	$2.83 \times 10^{-3}$	
150	FDM	$1.26 \times 10^{-2}$	$1.81 \times 10^{-2}$	$1.83 \times 10^{-2}$
	FD-MGDL	$8.07 \times 10^{-3}$	$8.07 \times 10^{-3}$	
200	FDM	$4.47 \times 10^{-1}$	$4.49 \times 10^{-1}$	$4.52 \times 10^{-1}$
	FD-MGDL	$5.20 \times 10^{-2}$	$5.21 \times 10^{-2}$	

Table 8: Performance comparison of FDM and FD-MGDL for the 3D Helmholtz problem (18) with the exact solution (19).

$\kappa$	Method	TrRSE	TeRSE	
			Trilinear	Triquadratic
20	FDM	$3.18 \times 10^{-2}$	$7.77 \times 10^{-2}$	$8.05 \times 10^{-2}$
	FD-MGDL	$2.74 \times 10^{-2}$	$3.31 \times 10^{-2}$	
30	FDM	$8.17 \times 10^{-3}$	$8.15 \times 10^{-2}$	$8.30 \times 10^{-2}$
	FD-MGDL	$1.69 \times 10^{-2}$	$1.81 \times 10^{-2}$	
40	FDM	$5.85 \times 10^{-1}$	$5.88 \times 10^{-1}$	$6.08 \times 10^{-1}$
	FD-MGDL	$3.13 \times 10^{-1}$	$3.28 \times 10^{-1}$	
50	FDM	$3.79 \times 10^{-1}$	$4.83 \times 10^{-1}$	$5.26 \times 10^{-1}$
	FD-MGDL	$3.48 \times 10^{-1}$	$3.91 \times 10^{-1}$	

## 7.2 Numerical Results and Analysis

Tables 6-9 summarize the FDM and FD-MGDL comparison results for the same model problems discussed in Sections 5-6. In particular, Table 6 reports FDM and FD-MGDL errors for the 2D Helmholtz equation (15) with the exact solution (16), Table 7 does the same for (15) with (17), while Tables 8 and 9 present the corresponding results for the 3D Helmholtz equation (18) with the exact solutions (19) and (20), respectively. For each case we include training RSE (TrRSE) measured at the grid nodes and testing RSE (TeRSE) reconstructed at off-grid test points using bilinear/trilinear and bi-/triquadratic interpolation, which facilitates a direct comparison between the nodal FDM solution and the mesh-free FD-MGDL reconstruction.

The limitations of FDM compared to the proposed FD-MGDL are summarized by two primary factors:

Table 9: Performance comparison of FDM and FD-MGDL for the 3D Helmholtz problem (18) with the exact solution (20).

$\kappa$	Method	TrRSE	TeRSE	
			Trilinear	Triquadratic
20	FDM	$6.10 \times 10^{-2}$	$1.01 \times 10^{-1}$	$1.03 \times 10^{-1}$
	FD-MGDL	$4.16 \times 10^{-2}$	$4.29 \times 10^{-2}$	
30	FDM	$3.45 \times 10^{-1}$	$4.02 \times 10^{-1}$	$4.23 \times 10^{-1}$
	FD-MGDL	$2.51 \times 10^{-1}$	$2.59 \times 10^{-1}$	

1. **Two-Stage Error Propagation.** FDM computes solutions exclusively at discrete grid nodes. Values at testing points must be estimated via interpolation, meaning the testing accuracy is coupled to both the discretization error and the interpolation error. As seen in Table 6 for  $\kappa = 50$ , even when the nodal (training) error is small, the testing error can be significantly higher. Furthermore, the transition to higher-order (quadratic) interpolation often yields only marginal improvements, highlighting the instability of this two-stage process.
2. **Grid Sensitivity and the Pollution Effect.** FDM’s ability to resolve oscillatory solutions is fundamentally constrained by grid spacing. If the mesh is too coarse to capture the high-frequency components, as observed for  $\kappa = 100$ , the method suffers from severe under-resolution and a dramatic loss of accuracy. This sensitivity is a hallmark of the pollution effect in high-frequency Helmholtz problems, where the required grid density to maintain accuracy grows nonlinearly with the wavenumber  $\kappa$ .

In contrast, FD-MGDL produces a mesh-free, continuous solution representation. Because it can be evaluated directly at any spatial location without secondary interpolation, the testing errors remain consistently stable and closely aligned with the training errors across all frequency regimes.

### 7.3 The Role of the Grid in FD-MGDL

It is essential to clarify that in FD-MGDL, the grid discretizes the loss function, not the solution space:

- **Training Phase:** The grid serves as a sampling strategy to construct residuals. Finite difference templates efficiently approximate the Laplacian, avoiding the computational overhead and spectral bias of automatic differentiation.
- **Inference Phase:** Once trained, the solution is a continuous function  $s_L^*(\mathbf{x})$  parameterized by the DNN. Forward propagation provides a solution at any spatial coordinate without requiring interpolation or post-processing.

While this study utilizes rectangular domains to establish efficiency, the framework is inherently extensible to complex geometries via two primary paths:

1. **Coordinate Transformation:** Mapping complex domains to a rectangular computational space allows the use of current structured stencils.
2. **Generalized Finite Difference (GFD):** Transitioning to unstructured “clouds of points” to define difference templates on arbitrary shapes.

## 8 Concave Model

In this section, we apply FD-MGDL to the concave velocity model governed by the two-dimensional Helmholtz equation [42], which involves variable wavenumbers in  $\mathbb{R}^2$ . Testing a concave velocity profile is scientifically significant because it introduces caustics and multipathing effects, where wave energy is focused into localized regions. This creates a high-stress scenario for numerical solvers, as they must accurately capture sharp phase transitions and amplitude spikes without introducing artificial oscillations.

Since analytical solutions for such non-homogeneous media are generally unavailable, numerical methods like finite difference and finite element methods are essential for validating the robustness of the solver. To truncate the unbounded domain while preventing non-physical reflections from contaminating the focused wavefield, absorbing boundary conditions are imposed; we adopt the perfectly matched layer (PML) introduced by Bérenger [43], leading to the Helmholtz equation with PML.

For this benchmark, our FD-MGDL method is built on the classical 5-point finite difference scheme, which is known to suffer from significant numerical dispersion. Since the exact solution is unavailable for this concave velocity model, we use the optimal 9-point scheme of Chen et al. [44] as a high-fidelity reference. This 9-point operator is designed to reduce dispersion and improve accuracy, serving as a reliable surrogate for the exact wavefield.

We compare the wavefields produced by the standard 5-point scheme, FD-MGDL, and the optimal 9-point reference to assess how effectively FD-MGDL reduces the dispersion errors of the 5-point baseline.

Specifically, we consider time-harmonic wave propagation in a heterogeneous medium governed by the 2D Helmholtz equation. For  $(x, y) \in \mathbb{R}^2$  with spatially varying velocity  $v(x, y)$  and source term  $g(x, y)$ , the wavefield  $u(x, y)$  satisfies:

$$(\Delta + \kappa^2)u(x, y) = g(x, y),$$

where  $\kappa(x, y) = \omega/v(x, y)$  is the spatially dependent wavenumber and  $\omega$  is the angular frequency.

The concave velocity model, illustrated in Figure 9, is defined on the square domain

$$\Omega := [0, 2000] \text{ m} \times [0, 2000] \text{ m}.$$

The model features three piecewise constant velocity layers: 1500 m/s, 2000 m/s, and 2500 m/s, ordered from top to bottom. A point source is positioned at  $(x_s, y_s) = (1000, 800)$ , characterized by

$$g(x, y) := \delta(x - x_s, y - y_s) \widehat{R}(f, f_0),$$

where  $\widehat{R}(f, f_0)$  is the frequency-domain Ricker wavelet with a dominant frequency  $f_0 = 25$  Hz:

$$\widehat{R}(f, f_0) = \int_{-\infty}^{+\infty} (1 - 2\pi^2 f_0^2 t^2) \exp(-\pi^2 f_0^2 t^2) \exp(-i2\pi ft) dt.$$

To determine the wavefield for this configuration, we solve the following frequency-domain equation:

$$\Delta u + \kappa^2 u = -\delta(x - x_s, y - y_s) \widehat{R}(f, f_0), \quad \text{in } \mathbb{R}^2.$$

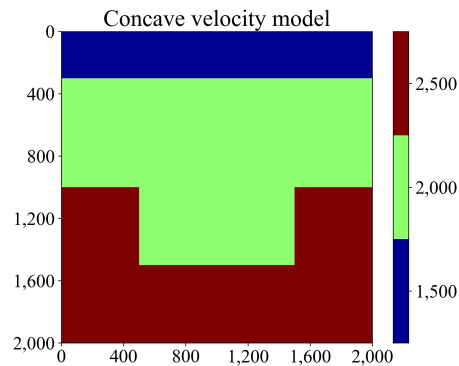


Figure 9: Three-layer concave velocity structure.

To truncate the computational domain and suppress artificial reflections, we apply the PML technique. The resulting Helmholtz equation with PML is given by:

$$\frac{\partial}{\partial x} \left( A \frac{\partial u}{\partial x} \right) + \frac{\partial}{\partial y} \left( B \frac{\partial u}{\partial y} \right) + C \kappa^2 u = -\delta(x - x_s, y - y_s) \widehat{R}(f, f_0),$$

where the complex-valued coefficients  $A$ ,  $B$ , and  $C$  are defined in terms of the stretching functions  $e_x$  and  $e_y$ :

$$A := \frac{e_y}{e_x}, \quad B := \frac{e_x}{e_y}, \quad C := e_x e_y.$$

The stretching functions  $e_x$  and  $e_y$  account for wave attenuation and are defined as:

$$e_x := 1 + i \frac{\sigma_x}{\omega}, \quad e_y := 1 + i \frac{\sigma_y}{\omega},$$

where  $\omega := 2\pi f$  is the angular frequency. To minimize numerical reflections at the interface, the damping profiles  $\sigma_x$  and  $\sigma_y$  are chosen as differentiable functions. Specifically, for the  $x$ -direction:

$$\sigma_x := \begin{cases} 2\pi a_0 f_0 \left( \frac{l_x}{L_{PML}} \right)^2, & \text{inside the PML,} \\ 0, & \text{outside the PML,} \end{cases}$$

where  $f_0$  is the dominant source frequency,  $L_{PML}$  is the layer thickness, and  $l_x$  represents the distance from the point  $(x, y)$  to the interior-PML interface. The scaling parameter  $a_0$  is set to 1.79 [45]. The function  $\sigma_y$  is defined analogously for the  $y$ -direction.

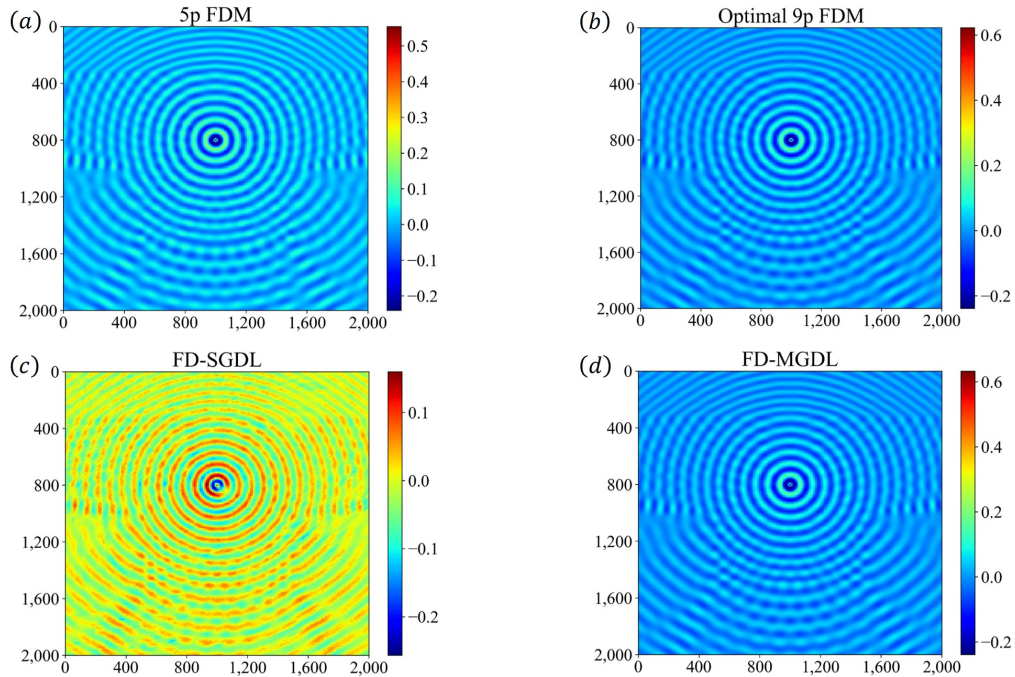


Figure 10: Wavefield comparison for the concave velocity model. Reference wavefields computed using the 5-point (a) and optimal 9-point (b) finite-difference schemes, and wavefields predicted by FD-SGDL (c) and FD-MGDL (d).

We evaluate the FD-MGDL-predicted wavefield by comparing it with solutions computed using two finite-difference frequency-domain (FDFD) methods: the classical 5-point scheme and the optimal 9-point scheme of [44].

On a  $201 \times 201$  grid, the real part of the monofrequency wavefield at  $f = 25Hz$  obtained with the 5-point and optimal 9-point schemes is shown in Figures 10 (a) and (b), respectively. Figures 10 (c) and (d) display the wavefields produced by FD-SGDL and FD-MGDL. Figure 11 shows the training loss versus epochs, confirming the convergence of FD-MGDL. Figures 12 (a)-(c) present the FD-MGDL predictions at grades 1–3, illustrating the progressive refinement across grades.

Because the optimal 9-point scheme achieves high accuracy and effectively reduces numerical dispersion, especially at large wavenumbers, we use it as the reference solution. It clearly captures upward and downward

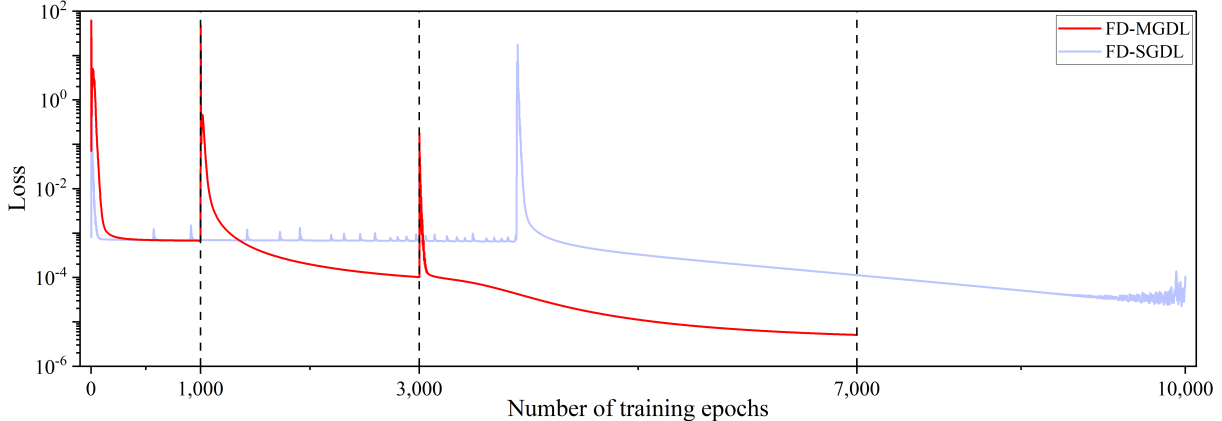


Figure 11: Training loss curves of FD-SGDL and FD-MGDL for the concave velocity model.

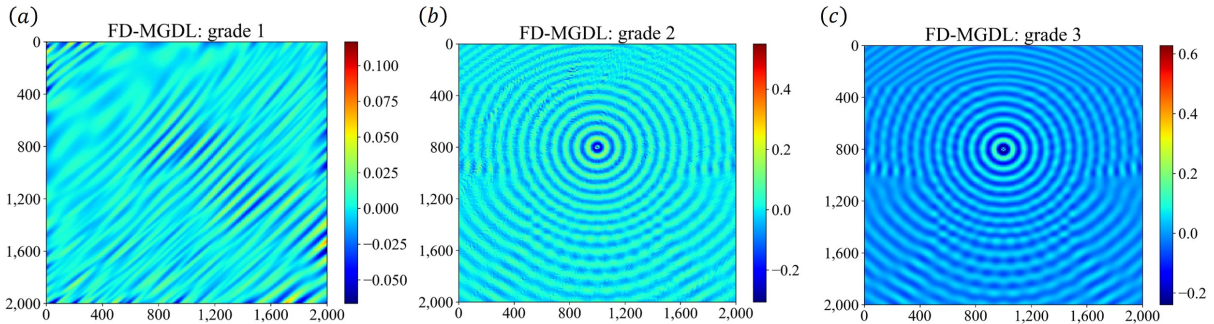


Figure 12: Wavefields predicted by FD-MGDL for the concave velocity model at successive grades: grade 1 (a), grade 2 (b), and grade 3 (c).

incident waves, transmitted waves, and reflections within the middle velocity layer consistent with Snell’s law. As seen in Figure 10, FD-MGDL closely matches the 9-point reference, whereas the 5-point scheme and FD-SGDL show noticeable discrepancies. These results demonstrate the improved accuracy of FD-MGDL.

We also compare computational efficiency. The total training time of FD-MGDL is 2,399 s, significantly shorter than FD-SGDL (10,150 s). This substantial reduction, together with improved accuracy, highlights the effectiveness and efficiency of FD-MGDL for wavefield simulation.

In summary, for the concave velocity benchmark, FD-MGDL significantly enhances wavefield accuracy compared with the 5-point scheme and FD-SGDL, closely matching the 9-point reference while effectively mitigating numerical dispersion. The grade-wise results show progressive refinement, and the method achieves higher accuracy with significantly shorter training time, demonstrating both effectiveness and efficiency for wavefield simulation in heterogeneous media.

## 9 Conclusion

This paper presented a novel adaptive algorithm, Finite Difference leveraged by Multi-Grade Deep Learning (FD-MGDL), designed to overcome the persistent challenges of solving high-frequency Helmholtz equations. By synergizing the structural robustness of finite difference discretization with the adaptive approximation power of multi-grade deep learning, the framework successfully mitigates the spectral bias and optimization stiffness inherent in traditional Physics-Informed Neural Networks (PINNs).

The core contributions and findings of this study are summarized as follows:

- **Unified Discrete Formulation:** By substituting automatic differentiation with a finite difference-based loss function, we transformed boundary conditions from soft penalty terms into hard constraints.

This architectural choice eliminates the destructive competition between PDE and boundary losses, substantially stabilizing the training process.

- **Adaptive Grade Refinement:** The MGDL strategy progressively enhances solution accuracy by introducing shallow layers grade-by-grade. We established a rigorous monotonicity theorem proving that the training loss remains non-increasing as new grades are added, providing a solid theoretical foundation for the adaptive stopping criterion.
- **Hybrid Architectural Design:** Our adaptive algorithm utilizes a specialized hybrid structure — employing sinusoidal activations in the initial grade to capture global oscillations and ReLU activations in subsequent grades to resolve irregular residuals. This approach ensures both high parameter efficiency and asymptotic consistency.
- **Superior Performance in High-Frequency Regimes:** Numerical experiments on 2D and 3D problems with wavenumbers up to  $\kappa = 200$  demonstrate that FD-MGDL consistently outperforms state-of-the-art baselines like Mscale, FBPINN, and SIREN in both accuracy and computational efficiency. Notably, FD-MGDL maintains stable training and well-controlled error distributions where traditional methods often diverge or stagnate due to the pollution effect.
- **Robustness in Inhomogeneous Media:** The application of FD-MGDL to a concave velocity model showcased its ability to accurately resolve complex physical phenomena, such as wave focusing and caustics, significantly surpassing standard finite difference schemes in stability and resolution.

A defining feature of the FD-MGDL framework is its ability to preserve the mesh-free advantage of neural solvers. Unlike classical finite difference methods that yield solutions only at discrete grid points, FD-MGDL produces a continuous representation defined over the entire domain. Although FD schemes are used to approximate derivatives during training, the resulting model is a continuous function that can be evaluated at any coordinate.

Future research will focus on extending this framework to unstructured domains and complex geometries. While the current study utilizes structured grids, the principles of MGDL can be generalized using “clouds of points” (as in Generalized Finite Difference Methods) or radial basis functions. Additionally, we aim to incorporate higher-order accuracy into the derivative approximations.

To illustrate the potential for enhanced precision, consider a second-order derivative approximation with  $O(h^4)$  accuracy. By utilizing a five-point central stencil—comprising  $x - 2h$ ,  $x - h$ ,  $x$ ,  $x + h$ , and  $x + 2h$ —the derivative is computed as:

$$u''(x) = \frac{1}{12h^2} [-u(x - 2h) + 16u(x - h) - 30u(x) + 16u(x + h) - u(x + 2h)] + O(h^4).$$

Integrating such higher-order schemes into the FD-MGDL loss function will allow for even greater reduction of the pollution effect in extreme high-frequency regimes. Ultimately, this adaptive multi-grade framework provides a robust and scalable path forward for solving complex, oscillatory partial differential equations in physics and engineering.

## Acknowledgments

Rui Wang is supported in part by the Natural Science Foundation of China under grants 12571562 and 12171202. Tingting Wu is supported by the Natural Science Foundation of Shandong Province of China under grant ZR2021MA 049. Yuesheng Xu is supported in part by the US National Science Foundation under grant DMS-2208386.

## A Proof of Theorem 1

*Proof.* For each grade  $l \in \mathbb{N}_{L-1}$ , the loss function, originally defined in (4) with  $\tilde{\mathcal{N}}_D := s_l$  and  $\Theta := \Theta_l$ , can be expressed using the discrete Helmholtz operator (6) and the discrete semi-norm (7) as

$$\mathcal{L}(s_l, \Theta_l) = \|f - \mathcal{A}_h s_l(\Theta_l; \cdot)\|_N^2,$$

We define the corresponding residual function by

$$e_l(\Theta_l; \mathbf{x}) := f(\mathbf{x}) - \mathcal{A}_h s_l(\Theta_l; \mathbf{x}), \quad \mathbf{x} \in \Omega.$$

Upon obtaining the optimal parameters  $\Theta_l^*$ , we denote the trained network and its residual by

$$s_l^*(\mathbf{x}) := s_l(\Theta_l^*; \mathbf{x}), \quad e_l^*(\mathbf{x}) := e_l(\Theta_l^*; \mathbf{x}) = f(\mathbf{x}) - \mathcal{A}_h s_l^*(\mathbf{x}), \quad \mathbf{x} \in \Omega.$$

Thus, the optimal loss simplifies to  $\mathcal{L}(s_l, \Theta_l^*) = \|e_l^*\|_N^2$ . To establish the desired inequality  $\mathcal{L}(s_{l+1}, \Theta_{l+1}^*) \leq \mathcal{L}(s_l, \Theta_l^*)$ , it suffices to prove  $\|e_{l+1}^*\|_N \leq \|e_l^*\|_N$ .

From the grade-wise construction (5), it follows that  $s_l^*(\mathbf{x}) = \sum_{i \in \mathbb{N}_l} g_i^*(\mathbf{x})$  for all  $\mathbf{x} \in \Omega$ . Consequently, at grade  $l+1$  we have

$$s_{l+1}(\Theta_{l+1}; \mathbf{x}) = s_l^*(\mathbf{x}) + g_{l+1}(\Theta_{l+1}; \mathbf{x}), \quad \mathbf{x} \in \Omega. \quad (21)$$

Substituting equation (21) into the definition of the residual  $e_{l+1}$  yields

$$e_{l+1}(\Theta_{l+1}; \mathbf{x}) = e_l^*(\mathbf{x}) - \mathcal{A}_h g_{l+1}(\Theta_{l+1}; \mathbf{x}), \quad \mathbf{x} \in \Omega, \quad (22)$$

with trainable parameters  $\Theta_{l+1}$ . Let  $\Theta_{l+1}^* := (\Theta_{l+1,1}^*, \Theta_{l+1,2}^*)$  denote the optimal parameters obtained by minimizing  $\mathcal{L}(s_{l+1}, \Theta_{l+1})$ . We then obtain from (22) that

$$e_{l+1}^*(\mathbf{x}) = e_l^*(\mathbf{x}) - \mathcal{A}_h g_{l+1}^*(\mathbf{x}), \quad \mathbf{x} \in \Omega. \quad (23)$$

Observe that  $(\Theta_{l+1,1}^*, \Theta_{l+1,2}^*) \in \mathcal{M}_{l+1,1} \times \mathcal{M}_{l+1,2}$  is a local minimizer of

$$F(\Theta_{l+1,1}, \Theta_{l+1,2}) := \|e_l^* - \mathcal{A}_h g_{l+1}((\Theta_{l+1,1}, \Theta_{l+1,2}); \cdot)\|_N^2.$$

Consequently, with  $\Theta_{l+1,1}^*$  fixed,  $\Theta_{l+1,2}^* \in \mathcal{M}_{l+1,2}$  is a local minimizer of  $F(\Theta_{l+1,1}^*, \Theta_{l+1,2})$ . By the definition of the linear operator  $\mathcal{Z}_{l+1}$ , the minimization of  $F(\Theta_{l+1,1}^*, \Theta_{l+1,2})$  over  $\Theta_{l+1,2} \in \mathcal{M}_{l+1,2}$  is equivalent to solving the convex optimization problem

$$\min_{\Theta_{l+1,2} \in \mathcal{M}_{l+1,2}} \|e_l^* - \mathcal{Z}_{l+1}(\Theta_{l+1,2})\|_N^2.$$

Thus,  $\Theta_{l+1,2}^* \in \mathcal{M}_{l+1,2}$ , being a local minimizer of this convex problem, is also a global minimizer. This implies that  $\mathcal{Z}_{l+1}(\Theta_{l+1,2}^*) = \mathcal{A}_h g_{l+1}^*$  is the best approximation to  $e_l^*$  from the linear space  $\mathcal{Z}_{l+1}(\mathcal{M}_{l+1,2})$  with respect to the semi-norm  $\|\cdot\|_N$ . Clearly, the zero function belongs to  $\mathcal{Z}_{l+1}(\mathcal{M}_{l+1,2})$ . Therefore, by the best-approximation property and equation (23), we conclude that

$$\|e_{l+1}^*\|_N = \|e_l^* - \mathcal{A}_h g_{l+1}^*\|_N \leq \|e_l^* - 0\|_N \leq \|e_l^*\|_N,$$

which proves the first assertion.

We next prove the second assertion regarding the equality condition. Clearly, the equality  $\mathcal{L}(s_{l+1}, \Theta_{l+1}^*) = \mathcal{L}(s_l, \Theta_l^*)$  holds if and only if

$$\|e_l^* - \mathcal{A}_h g_{l+1}^*\|_N = \|e_l^* - 0\|_N. \quad (24)$$

Recall that  $\mathcal{A}_h g_{l+1}^*$  is the best approximation to  $e_l^*$  from the linear space  $\mathcal{Z}_{l+1}(\mathcal{M}_{l+1,2})$  with respect to the semi-norm  $\|\cdot\|_N$ . Thus, equality (24) holds if and only if the zero function is a best approximation to  $e_l^*$  from that subspace. It remains to show that the latter is equivalent to  $\|\mathcal{A}_h g_{l+1}^*\|_N = 0$ . By similar arguments used in the proof of Lemma 7 in [30], if the zero function is a best approximation to  $e_l^*$ , then there holds that  $\|\mathcal{A}_h g_{l+1}^* - 0\|_N = 0$ , that is  $\|\mathcal{A}_h g_{l+1}^*\|_N = 0$ . Conversely, if  $\|\mathcal{A}_h g_{l+1}^*\|_N = 0$ , then by the triangle inequality of the semi-norm, we obtain that

$$\|e_l^* - 0\|_N \leq \|e_l^* - \mathcal{A}_h g_{l+1}^*\|_N + \|\mathcal{A}_h g_{l+1}^*\|_N = \|e_l^* - \mathcal{A}_h g_{l+1}^*\|_N,$$

which yields that the zero function is a best approximation to  $e_l^*$ .  $\square$

## B Proof of Theorem 2

*Proof.* We first prove statement (1). Let  $\{\mathbf{w}_{lj}, \alpha_{lj}\}_{j=1}^{m_l}$  be any feasible solution to the non-convex (8). As shown previously, we can associate with this solution a corresponding feasible solution  $\{\mathbf{v}_{li}, \mathbf{u}_{li}\}_{i=1}^{P_l}$  to the convex problem (13) that satisfies

$$\left\| \mathbf{e}_{l-1}^* - \mathcal{A}_h \sum_{j=1}^{m_l} (\mathbf{X}_l \mathbf{w}_{lj})_+ \alpha_{lj} \right\|_2^2 = \left\| \mathbf{e}_{l-1}^* - \mathcal{A}_h \sum_{i=1}^{P_l} \mathbf{D}_{li} \mathbf{X}_l (\mathbf{v}_{li} - \mathbf{u}_{li}) \right\|_2^2.$$

That is, the feasible solution  $\{\mathbf{v}_{li}, \mathbf{u}_{li}\}_{i=1}^{P_l}$  of (13) achieves exactly the same objective value as the original non-convex solution  $\{\mathbf{w}_{lj}, \alpha_{lj}\}_{j=1}^{m_l}$  of (8). Since every feasible solution of (8) can be mapped to a feasible solution of (13) with the same objective value, taking minima over both problems yields that  $P_{\text{nc}}^* \geq P_c^*$ .

We next verify statement (2). Suppose that  $\{\mathbf{v}_{li}^*, \mathbf{u}_{li}^*\}_{i=1}^{P_l}$  is an optimal solution of problem (13) and define

$$m_l^* := \sum_{i=1}^{P_l} (1[\mathbf{v}_{li}^* \neq 0] + 1[\mathbf{u}_{li}^* \neq 0]).$$

Using this optimal solution, We construct a feasible solution for the non-convex problem (8) as follows. For each  $i \in \mathbb{N}_{P_l}$ ,

- if  $\mathbf{v}_{li}^* \neq 0$ , we introduce a neuron with parameters

$$\mathbf{w}_{lj_{1,i}}^* = \frac{\mathbf{v}_{li}^*}{\|\mathbf{v}_{li}^*\|}, \quad \alpha_{lj_{1,i}}^* = \|\mathbf{v}_{li}^*\|;$$

- if  $\mathbf{u}_{li}^* \neq 0$ , we introduce a neuron with parameters

$$\mathbf{w}_{lj_{2,i}}^* = \frac{\mathbf{u}_{li}^*}{\|\mathbf{u}_{li}^*\|}, \quad \alpha_{lj_{2,i}}^* = -\|\mathbf{u}_{li}^*\|.$$

The indices  $j_{1,i}$  and  $j_{2,i}$  are taken distinct for different pairs, and the remaining  $m_l - m_l^*$  neurons are set to  $(\mathbf{0}, 0)$ . Because  $\{\mathbf{v}_{li}^*, \mathbf{u}_{li}^*\}_{i=1}^{P_l}$  satisfies the constraint condition of (13), we have for each  $i \in \mathbb{N}_{P_l}$  that

$$(\mathbf{X}_l \mathbf{w}_{lj_{1,i}}^*)_+ = \mathbf{D}_{li} \mathbf{X}_l \mathbf{w}_{lj_{1,i}}^*, \quad (\mathbf{X}_l \mathbf{w}_{lj_{2,i}}^*)_+ = \mathbf{D}_{li} \mathbf{X}_l \mathbf{w}_{lj_{2,i}}^*. \quad (25)$$

Denote the constructed parameters by  $\{(\mathbf{w}_{lj}^*, \alpha_{lj}^*)\}_{j=1}^{m_l}$ . Then the output of the two-layer network equals

$$\sum_{j=1}^{m_l} (\mathbf{X}_l \mathbf{w}_{lj}^*)_+ \alpha_{lj}^* = \sum_{i=1}^{P_l} (\mathbf{X}_l \mathbf{w}_{lj_{1,i}}^*)_+ \alpha_{lj_{1,i}}^* + (\mathbf{X}_l \mathbf{w}_{lj_{2,i}}^*)_+ \alpha_{lj_{2,i}}^*.$$

Substituting (25) into the above equation yields that

$$\sum_{j=1}^{m_l} (\mathbf{X}_l \mathbf{w}_{lj}^*)_+ \alpha_{lj}^* = \sum_{i=1}^{P_l} \left( \mathbf{D}_{li} \mathbf{X}_l \mathbf{w}_{lj_{1,i}}^* \alpha_{lj_{1,i}}^* + \mathbf{D}_{li} \mathbf{X}_l \mathbf{w}_{lj_{2,i}}^* \alpha_{lj_{2,i}}^* \right).$$

Using the definitions of  $\mathbf{w}_{lj_{1,i}}^*, \alpha_{lj_{1,i}}^*$  and  $\mathbf{w}_{lj_{2,i}}^*, \alpha_{lj_{2,i}}^*$ , we obtain that

$$\sum_{j=1}^{m_l} (\mathbf{X}_l \mathbf{w}_{lj}^*)_+ \alpha_{lj}^* = \sum_{i=1}^{P_l} \mathbf{D}_{li} \mathbf{X}_l (\mathbf{v}_{li}^* - \mathbf{u}_{li}^*).$$

Therefore,  $\{(\mathbf{w}_{lj}^*, \alpha_{lj}^*)\}_{j=1}^{m_l}$  is a feasible solution to (8), whose objective value equals the optimal value  $P_c^*$ . Consequently,  $P_{\text{nc}}^* \leq P_c^*$ . Combined with  $P_{\text{nc}}^* \geq P_c^*$  from statement (1), we get  $P_{\text{nc}}^* = P_c^*$ .  $\square$

## C Detailed Experimental Configurations

This appendix provides a comprehensive summary of the experimental configurations used throughout the paper. The eight tables below compile the detailed hyperparameter settings of all compared methods, including network architectures, activation functions, learning rate schedules, and training epochs.

FD-MGDL employs the adaptive FD-MGDL algorithm, in which the number of grades is automatically determined according to the problem difficulty. In all experiments, the first grade uses a shallow network with two hidden layers and sin activation, while each subsequent grade consists of a single hidden layer with ReLU activation. The width of all hidden layers in FD-MGDL is fixed at 256. The hyperparameter settings for FD-MGDL in the four experiments across different wavenumbers  $\kappa$  are summarized in Tables 10, 12, 14, 16, which detail the grade-wise configurations used in the adaptive training process. The corresponding settings for the remaining comparison methods are provided in Tables 11, 13, 15, 17.

Table 10: Hyperparameter settings of FD-MGDL for the 2D Helmholtz problem (15) with the exact solution (16).

$\kappa$	Grade	$t_{\max}$	$t_{\min}$	Epochs
50	6	$\{10^{-1}, 10^{-2}, 10^{-3}, 10^{-3}, 10^{-3}, 10^{-3}\}$	$\{10^{-2}, 10^{-3}, 10^{-4}, 10^{-3}, 10^{-3}, 10^{-3}\}$	[400,3000,3000,2500,2500,1000]
100	4	$\{10^{-1}, 10^{-1}, 10^{-2}, 10^{-2}\}$	$\{10^{-1}, 10^{-2}, 10^{-3}, 10^{-3}\}$	[500,2000,2000,2000]
150	5	$\{10^{-1}, 10^{-1}, 10^{-2}, 10^{-3}, 10^{-2}\}$	$\{10^{-2}, 10^{-1}, 10^{-3}, 10^{-3}, 10^{-3}\}$	[500,1500,2000,2000,2000]
200	4	$\{10^{-1}, 10^{-1}, 10^{-3}, 10^{-2}\}$	$\{10^{-1}, 10^{-2}, 10^{-3}, 10^{-3}\}$	[500,2000,2000,2000]

Table 11: Hyperparameter settings of FD-SGDL, Mscale, FBPINN, SIREN, PINN and Pre-PINN for the 2D Helmholtz problem (15) with the exact solution (16).

$\kappa$	Method	Architecture (width $\times$ depth)	Activation	$\{t_{\max}, t_{\min}\}$ / Epochs
50	FD-SGDL, PINN, Pre-PINN	$256 \times 7$	$\sin \times 2 + \text{ReLU} \times 5$	$\{10^{-3}, 10^{-4}\} / 15,000$
	SIREN	$256 \times 7$	$\sin \times 7$	$\{10^{-3}, 10^{-4}\} / 15,000$
	Mscale	$180 \times 3$ with scales $\{1, 2, 4, 8, 16, 32\}$	$\sin \times 3$	$\{10^{-3}, -\} / 15,000$
	FBPINN	$40 \times 2$ with subdomains $15 \times 15$	$\tanh \times 2$	$\{10^{-3}, -\} / 15,000$
100	FD-SGDL, PINN, Pre-PINN	$256 \times 5$	$\sin \times 2 + \text{ReLU} \times 3$	$\{10^{-2}, -\} / 8,000$
	SIREN	$256 \times 5$	$\sin \times 5$	$\{10^{-2}, -\} / 8,000$
	Mscale	$160 \times 3$ with scales $\{1, 2, 4, 8, 16\}$	$\sin \times 3$	$\{10^{-3}, -\} / 8,000$
	FBPINN	$40 \times 2$ with subdomains $12 \times 12$	$\tanh \times 2$	$\{10^{-3}, -\} / 8,000$
150	FD-SGDL, PINN, Pre-PINN	$256 \times 6$	$\sin \times 2 + \text{ReLU} \times 4$	$\{10^{-2}, 10^{-4}\} / 10,000$
	SIREN	$256 \times 6$	$\sin \times 6$	$\{10^{-2}, 10^{-4}\} / 10,000$
	Mscale	$150 \times 3$ with scales $\{1, 2, 4, 8, 16, 32, 64\}$	$\sin \times 3$	$\{5 \times 10^{-4}, -\} / 10,000$
	FBPINN	$38 \times 2$ with subdomains $14 \times 14$	$\tanh \times 2$	$\{10^{-3}, -\} / 10,000$
200	FD-SGDL, PINN, Pre-PINN	$256 \times 5$	$\sin \times 2 + \text{ReLU} \times 3$	$\{10^{-2}, 10^{-4}\} / 8,000$
	SIREN	$256 \times 5$	$\sin \times 5$	$\{10^{-2}, 10^{-4}\} / 8,000$
	Mscale	$135 \times 3$ with scales $\{1, 2, 4, 8, 16, 32, 64\}$	$\sin \times 3$	$\{5 \times 10^{-4}, -\} / 8,000$
	FBPINN	$38 \times 2$ with subdomains $13 \times 13$	$\tanh \times 2$	$\{10^{-3}, -\} / 8,000$

## References

- [1] Maziar Raissi, Paris Perdikaris, and George E. Karniadakis. Physics-informed neural networks: A deep learning framework for solving forward and inverse problems involving nonlinear partial differential equations. *J. Comput. Phys.*, 378:686–707, 2019.
- [2] Zongyi Li, Nikola Kovachki, Kamyar Azizzadenesheli, Burigede Liu, Kaushik Bhattacharya, Andrew Stuart, and Anima Anandkumar. Fourier neural operator for parametric partial differential equations. In *Int. Conf. Learn. Represent.*, 2021.

Table 12: Hyperparameter settings of FD-MGDL for the 2D Helmholtz problem (15) with the exact solution (17).

$\kappa$	Grade	$t_{\max}$	$t_{\min}$	Epochs
50	3	$\{10^{-1}, 10^{-3}, 10^{-1}\}$	$\{10^{-1}, 10^{-4}, 10^{-3}\}$	[500,2000,2000]
100	4	$\{10^{-1}, 10^{-2}, 10^{-3}, 10^{-3}\}$	$\{10^{-2}, 10^{-3}, 10^{-4}, 10^{-4}\}$	[500,2000,2000,2000]
150	3	$\{10^{-1}, 10^{-2}, 10^{-3}\}$	$\{10^{-2}, 10^{-3}, 10^{-3}\}$	[500,1000,1000]
200	4	$\{10^{-1}, 10^{-1}, 10^{-3}, 10^{-2}\}$	$\{10^{-2}, 10^{-2}, 10^{-4}, 10^{-2}\}$	[500,1000,1000,1000]

Table 13: Hyperparameter settings of FD-SGDL, Mscale and FBPINN for the 2D Helmholtz problem (15) with the exact solution (17).

$\kappa$	Method	Architecture (width $\times$ depth)	Activation	$\{t_{\max}, t_{\min}\}$ / Epochs
50	FD-SGDL	$256 \times 4$	$\sin \times 2 + \text{ReLU} \times 2$	$\{10^{-1}, 10^{-4}\}$ / 6,000
	Mscale	$140 \times 3$ with scales $\{1, 2, 4, 8, 16\}$	$\sin \times 3$	$\{5 \times 10^{-4}, -\}$ / 6,000
	FBPINN	$32 \times 2$ with subdomains $13 \times 13$	$\tanh \times 2$	$\{10^{-3}, -\}$ / 6,000
100	FD-SGDL	$256 \times 5$	$\sin \times 2 + \text{ReLU} \times 3$	$\{10^{-1}, 10^{-2}\}$ / 8,000
	Mscale	$160 \times 3$ with scales $\{1, 2, 4, 8, 16\}$	$\sin \times 3$	$\{5 \times 10^{-4}, -\}$ / 8,000
	FBPINN	$32 \times 2$ with subdomains $15 \times 15$	$\tanh \times 2$	$\{10^{-3}, -\}$ / 8,000
150	FD-SGDL	$256 \times 4$	$\sin \times 2 + \text{ReLU} \times 2$	$\{10^{-1}, 10^{-4}\}$ / 5,000
	Mscale	$120 \times 3$ with scales $\{1, 2, 4, 8, 16, 32, 64\}$	$\sin \times 3$	$\{5 \times 10^{-4}, -\}$ / 5,000
	FBPINN	$32 \times 2$ with subdomains $13 \times 13$	$\tanh \times 2$	$\{10^{-3}, -\}$ / 5,000
200	FD-SGDL	$256 \times 5$	$\sin \times 2 + \text{ReLU} \times 3$	$\{10^{-1}, 10^{-2}\}$ / 5,000
	Mscale	$164 \times 3$ with scales $\{1, 2, 4, 8, 16\}$	$\sin \times 3$	$\{5 \times 10^{-4}, -\}$ / 5,000
	FBPINN	$32 \times 2$ with subdomains $15 \times 15$	$\tanh \times 2$	$\{10^{-3}, -\}$ / 5,000

Table 14: Hyperparameter settings of FD-MGDL for the 3D Helmholtz problem (18) with the exact solution (19).

$\kappa$	Grade	$t_{\max}$	$t_{\min}$	Epochs
20	5	$\{10^{-1}, 10^{-2}, 10^{-3}, 10^{-3}, 10^{-3}\}$	$\{10^{-1}, 10^{-3}, 10^{-4}, 10^{-3}, 10^{-3}\}$	[500,2000,2000,2000,2000]
30	3	$\{10^{-1}, 10^{-2}, 10^{-3}\}$	$\{10^{-1}, 10^{-4}, 10^{-4}\}$	[500,2500,3000]
40	7	$\{10^{-1}, 10^{-1}, 10^{-3}(\times 5)\}$	$\{10^{-1}, 10^{-1}, 10^{-3}(\times 5)\}$	[500, 2000, 2000( $\times 5$ )]
50	4	$\{10^{-1}, 10^{-2}, 10^{-3}, 10^{-3}\}$	$\{10^{-1}, 10^{-3}, 10^{-4}, 10^{-4}\}$	[500,2000,2000,2000]

Table 15: Hyperparameter settings of FD-SGDL, Mscale and FBPINN for the 3D Helmholtz problem (18) with the exact solution (19).

$\kappa$	Method	Architecture (width $\times$ depth)	Activation	$\{t_{\max}, t_{\min}\}$ / Epochs
20	FD-SGDL	$256 \times 6$	$\sin \times 2 + \text{ReLU} \times 4$	$\{10^{-3}, -\}$ / 10,000
	Mscale	$164 \times 3$ with scales $\{1, 2, 4, 8, 16, 32\}$	$\sin \times 3$	$\{3 \times 10^{-4}, -\}$ / 10,000
	FBPINN	$40 \times 2$ with subdomains $5 \times 6 \times 6$	$\tanh \times 2$	$\{10^{-3}, -\}$ / 10,000
30	FD-SGDL	$256 \times 4$	$\sin \times 2 + \text{ReLU} \times 2$	$\{10^{-1}, 10^{-2}\}$ / 8,000
	Mscale	$127 \times 3$ with scales $\{1, 2, 4, 8, 16, 32\}$	$\sin \times 3$	$\{3 \times 10^{-4}, -\}$ / 8,000
	FBPINN	$37 \times 2$ with subdomains $5 \times 5 \times 5$	$\tanh \times 2$	$\{10^{-3}, -\}$ / 8,000
40	FD-SGDL	$256 \times 8$	$\sin \times 2 + \text{ReLU} \times 6$	$\{10^{-2}, 10^{-3}\}$ / 15,000
	Mscale	$168 \times 3$ with scales $\{1, 2, 4, 8, 16, 32, 64, 128\}$	$\sin \times 3$	$\{2 \times 10^{-4}, -\}$ / 15,000
	FBPINN	[43, 44] with subdomains $6 \times 6 \times 6$	$\tanh \times 2$	$\{10^{-3}, -\}$ / 15,000
50	FD-SGDL	$256 \times 5$	$\sin \times 2 + \text{ReLU} \times 3$	$\{10^{-2}, -\}$ / 8,000
	Mscale	$147 \times 3$ with scales $\{1, 2, 4, 8, 16, 32\}$	$\sin \times 3$	$\{2 \times 10^{-4}, -\}$ / 8,000
	FBPINN	$43 \times 2$ with subdomains $5 \times 5 \times 5$	$\tanh \times 2$	$\{10^{-3}, -\}$ / 8,000

Table 16: Hyperparameter settings of FD-MGDL for the 3D Helmholtz problem (18) with the exact solution (20).

$\kappa$	Grade	$t_{\max}$	$t_{\min}$	Epochs
20	4	$\{10^{-1}, 10^{-1}, 10^{-3}, 10^{-3}\}$	$\{10^{-2}, 10^{-1}, 10^{-3}, 10^{-3}\}$	[500,1000,1000,1000]
30	4	$\{10^{-1}, 10^{-1}, 10^{-2}, 10^{-3}\}$	$\{10^{-4}, 10^{-1}, 10^{-3}, 10^{-4}\}$	[500,1000,1000,1000]

Table 17: Hyperparameter settings of FD-SGDL, Mscale and FBPINN for the 3D Helmholtz problem (18) with the exact solution (20).

$\kappa$	Method	Architecture (width $\times$ depth)	Activation	$\{t_{\max}, t_{\min}\}$ / Epochs
20	FD-SGDL	$256 \times 5$	$\sin \times 2 + \text{ReLU} \times 3$	$\{10^{-1}, 10^{-3}\} / 5,000$
	Mscale	$147 \times 3$ with scales $\{1, 2, 4, 8, 16, 32\}$	$\sin \times 3$	$\{2 \times 10^{-4}, -\} / 5,000$
	FBPINN	$32 \times 2$ with subdomains $6 \times 6 \times 6$	$\tanh \times 2$	$\{10^{-3}, -\} / 5,000$
30	FD-SGDL	$256 \times 5$	$\sin \times 2 + \text{ReLU} \times 3$	$\{10^{-1}, 10^{-2}\} / 5,000$
	Mscale	$147 \times 3$ with scales $\{32, 32, 32, 32, 32, 32\}$	$\sin \times 3$	$\{10^{-4}, -\} / 5,000$
	FBPINN	$32 \times 2$ with subdomains $6 \times 6 \times 6$	$\tanh \times 2$	$\{10^{-3}, -\} / 5,000$

- [3] Weinan E, Jiequn Han, and Arnulf Jentzen. Deep learning-based numerical methods for high-dimensional parabolic partial differential equations and backward stochastic differential equations. *Commun. Math. Stat.*, 5 (4):349–380, 2017.
- [4] Jiequn Han, Arnulf Jentzen, and Weinan E. Solving high-dimensional partial differential equations using deep learning. *Proc. Natl. Acad. Sci. USA*, 115 (34):8505–8510, 2018.
- [5] Weinan E and Bing Yu. The deep ritz method: A deep learning-based numerical algorithm for solving variational problems. *Commun. Math. Stat.*, 6 (1):1–12, 2018.
- [6] Justin Sirignano and Konstantinos Spiliopoulos. Dgm: A deep learning algorithm for solving partial differential equations. *J. Comput. Phys.*, 375:1339–1364, 2018.
- [7] Nikola Kovachki, Zongyi Li, Burigede Liu, Kamyar Azizzadenesheli, Kaushik Bhattacharya, Andrew Stuart, and Anima Anandkumar. Neural operator: Learning maps between function spaces with applications to pdes. *J. Mach. Learn. Res.*, 24 (89):1–97, 2023.
- [8] Ziqi Liu, Wei Cai, and Zhi-Qin John Xu. Multi-scale deep neural network (mscalednn) for solving poisson-boltzmann equation in complex domains. *Commun. Comput. Phys.*, 28 (5):1970–2001, 2020.
- [9] Wei Xiong, Xiaomeng Huang, Ziyang Zhang, Ruixuan Deng, Pei Sun, and Yang Tian. Koopman neural operator as a mesh-free solver of non-linear partial differential equations. *J. Comput. Phys.*, 513:113194, 2024.
- [10] Andy L Yang. A novel deep neural network algorithm for the helmholtz scattering problem in the unbounded domain. *Int. J. Numer. Anal. Mod.*, 20 (5):724–738, 2023.
- [11] Andy L Yang and Feng Gu. A mesh-less, ray-based deep neural network method for the helmholtz equation with high frequency. *Int. J. Numer. Anal. Mod.*, 19 (4):587–601, 2022.
- [12] Tak Shing Au Yeung, Ka Chun Cheung, Eric T. Chung, Shubin Fu, and Jianliang Qian. Learning rays via deep neural network in a ray-based ipdg method for high-frequency helmholtz equations in inhomogeneous media. *J. Comput. Phys.*, 465:111380, 2022.
- [13] Yael Azulay and Eran Treister. Multigrid-augmented deep learning preconditioners for the helmholtz equation. *SIAM J. Sci. Comput.*, 45 (3):S127–S151, 2022.
- [14] Sourabh Dogra, Lokendra Singh, Aditya Nigam, and Arpan Gupta. A deep learning-based approach for the inverse design of the helmholtz resonators. *Mater. Today Commun.*, 37:107439, 2023.

- [15] Junwoo Cho, Seungtae Nam, Hyunmo Yang, Seok-Bae Yun, Youngjoon Hong, and Eunbyung Park. Separable physics-informed neural networks. *Adv. Neural Inf. Process. Syst.*, 36:23761–23788, 2023.
- [16] Stefan Schoder and Florian Kraxberger. Feasibility study on solving the helmholtz equation in 3d with pinns. *arXiv preprint, arXiv:2403.06623*, 2024.
- [17] Jorge F. Urbán, Petros Stefanou, and José A. Pons. Unveiling the optimization process of physics informed neural networks: how accurate and competitive can pinns be. *J. Comput. Phys.*, 523:113656, 2025.
- [18] Sifan Wang, Yujun Teng, and Paris Perdikaris. Understanding and mitigating gradient flow pathologies in physics-informed neural networks. *SIAM J. Sci. Comput.*, 43 (5):A3055–A3081, 2021.
- [19] Yuesheng Xu. Multi-grade deep learning. *Com. Appl. Math. Comput.*, 2025.
- [20] Yuesheng Xu. Successive affine learning for deep neural networks. *Anal. Appl.*, 23 (08):1425–1467, 2025.
- [21] Ronglong Fang and Yuesheng Xu. Addressing spectral bias of deep neural networks by multi-grade deep learning. *Adv. Neural Inf. Process. Syst.*, 37:114122–114146, 2024.
- [22] Jie Jiang and Yuesheng Xu. Deep neural network solutions for oscillatory fredholm integral equations. *J. Integr. Equations Appl.*, 36 (1):23–55, 2024.
- [23] Jianhuan Cen and Qingsong Zou. Deep finite volume method for partial differential equations. *J. Comput. Phys.*, 517:113307, 2024.
- [24] Xingyu Chen, Jianhuan Cen, and Qingsong Zou. Adaptive trajectories sampling for solving pdes with deep learning methods. *Appl. Math. Comput.*, 481:128928, 2024.
- [25] Zhiwei Gao, Liang Yan, and Tao Zhou. Failure-informed adaptive sampling for pinns. *SIAM J. Sci. Comput.*, 45 (4):A1971–A1994, 2023.
- [26] Dehao Liu and Yan Wang. A dual-dimer method for training physics-constrained neural networks with minimax architecture. *Neural Netw.*, 136:112–125, 2021.
- [27] Zixue Xiang, Wei Peng, Xu Liu, and Wen Yao. Self-adaptive loss balanced physics-informed neural networks. *Neurocomputing*, 496:11–34, 2022.
- [28] Sifan Wang, Xinling Yu, and Paris Perdikaris. When and why pinns fail to train: A neural tangent kernel perspective. *J. Comput. Phys.*, 449:110768, 2022.
- [29] Taishan Zeng and Yuesheng Xu. Multi-grade deep learning for partial differential equations with applications to the burgers equation. *arXiv preprint, arXiv:2309.07401*, 2023.
- [30] Jie Jiang and Yuesheng Xu. Adaptive multi-grade deep learning for highly oscillatory fredholm integral equations of the second kind. *J. Sci. Comput.*, 106:64, 2026.
- [31] Vincent Sitzmann, Julien N. P. Martel, Alexander W. Bergman, David B. Lindell, and Gordon Wetzstein. Implicit neural representations with periodic activation functions. *Adv. Neural Inf. Process. Syst.*, 33:7462–7473, 2020.
- [32] W. Wu, G. Feng, Z. Li, and Y. Xu. Deterministic convergence of an online gradient method for bp neural networks. *IEEE Transactions on Neural Networks*, 16 (3):533–540, 2005.
- [33] Ronglong Fang and Yuesheng Xu. Computational advantages of multi-grade deep learning: Convergence analysis and performance insights. *arXiv preprint, arXiv:2507.20351*, 2025.
- [34] Mert Pilanci and Tolga Ergen. Neural networks are convex regularizers: exact polynomial-time convex optimization formulations for two-layer networks. In *International Conference on Machine Learning, PMLR*, pages 7695–7705, 2020.

- [35] Tolga Ergen and Mert Pilanci. Convex geometry and duality of over-parameterized neural networks. *J. Mach. Learn. Res.*, 22 (212):1–63, 2021.
- [36] Shijun Zhang, Zuowei Shen, and Yuesheng Xu. Multigrade neural network approximation. *arXiv preprint, arXiv:2601.16884*, 2026.
- [37] Ben Moseley, Andrew Markham, and Tarje Nissen-Meyer. Finite basis physics-informed neural networks (fbpinns): a scalable domain decomposition approach for solving differential equations. *Adv. Comput. Math.*, 49 (4):62, 2023.
- [38] Tim De Ryck, Florent Bonnet, Siddhartha Mishra, and Emmanuel de Bézenac. An operator preconditioning perspective on training in physics-informed machine learning. *Proc. Int. Conf. Learn. Represent.*, pages 54886–54914, 2024.
- [39] Zhongying Chen, Dongsheng Cheng, and Tingting Wu. A dispersion minimizing finite difference scheme and preconditioned solver for the 3d helmholtz equation. *J. Comput. Phys.*, 231 (24):8152–8175, 2012.
- [40] Tingting Wu. A dispersion minimizing compact finite difference scheme for the 2d helmholtz equation. *J. Comput. Appl. Math.*, 311:497–512, 2017.
- [41] Tingting Wu, Yuran Sun, and Dongsheng Cheng. A new finite difference scheme for the 3d helmholtz equation with a preconditioned iterative solver. *Appl. Numer. Math.*, 161:348–371, 2021.
- [42] Haoran Ren, Huazhong Wang, and Ting Gong. Seismic modeling of scalar seismic wave propagation with finite-difference scheme in frequency-space domain. *Geophys. Prospect. Pet.*, 48 (1):20–26, 2009.
- [43] Jean-Pierre Bérenger. A perfectly matched layer for the absorption of electromagnetic waves. *J. Comput. Phys.*, 114 (2):185–200, 1994.
- [44] Zhongying Chen, Dongsheng Cheng, Wei Feng, and Tingting Wu. An optimal 9-point finite difference scheme for the helmholtz equation with pml. *Int. J. Numer. Anal. Mod.*, 10 (2):389–410, 2013.
- [45] Yan Qing Zeng, J. Q. He, and Qing Huo Liu. The application of the perfectly matched layer in numerical modeling of wave propagation in poroelastic media. *Geophysics*, 66 (4):1258–1266, 2001.